Applications of deformable image registration: automatic segmentation and adaptive radiation therapy

Marc Morcos

Master of Science

Medical Physics Unit

McGill University

Montreal, Quebec

August 2011

A thesis submitted to the Faculty of Graduate Studies and Research of McGill University in partial fulfillment of the requirements of the degree of Master of Science

DEDICATION

To my family, without whom none of this would have been possible due to all their love, support and motivation.

ACKNOWLEDGEMENTS

I would like to start by thanking my supervisors, **Dr. François Deblois** and **Dr. Gabriela Stroian**, for their invaluable support throughout the year. Their guidance and encouragement at all stages of this project made it a wonderful experience.

I would like to acknowledge **Isabelle Lavoie** for the many hours spent carefully contouring patient CT sets and for all the helpful discussions on dosimetry, **Dr. Issam El Naqa** for his guidance with respect to deformable image registration as well as **Jonathan Thebaut** and **Joseph Holmes** for teaching me about clinical medical physics.

Among the students at the Medical Physics Unit, I would like to thank **Ellis Mitrou** for useful discussions and advice on countless topics concerning this work and **Andrew Alexander** for introducing me to the rewarding field of Medical Physics.

I am very grateful for the financial support I received from the ministère de la Santé et des Services sociaux (MSSS) of Quebec and the Weekend to End Breast Cancer (WEBC) research fund.

ABSTRACT

The contents of this thesis are best divided into two components: (*i*) evaluation of atlas-based segmentation and deformable contour propagation and (*ii*) adaptive radiation therapy using deformable electron density mapping. The first component of this thesis involves the evaluation of two commercial deformable registration systems with respect to automatic segmentation techniques. Overall, the techniques revealed that manual modifications would be required if the structures were to be used for treatment planning. The automatic segmentation methods utilized by both commercial products serve as an excellent starting point for contouring process and also reduce inter- and intra-physician variability when contouring.

In the second component, we developed a framework for dose accumulation adaptive radiation therapy. By registering the planning computed tomography (CT) images to the weekly cone-beam computed tomography (CBCT) images, we were able to produce modified CBCT images which possessed CT Hounsfield units; this was achieved by using deformable image registration. Dose distributions were recalculated onto the modified CBCT images and then compared to the planned dose distributions. Results indicated that deformable electron density mapping is a feasible technique to allow dose distributions to be recalculated on pre-treatment CBCT scans.

ABRÉGÉ

Le contenu de cette thèse est divisé en deux partis: (i) l'évaluation de la segmentation automatique basée sur des atlas anatomiques numériques et la propagation des structures déformables et (ii) la radiothérapie adaptative déformable utilisant la cartographie de la densité électronique. Le premier élément de cette thèse comprend l'évaluation de deux logiciels commerciaux par rapport aux techniques de segmentation automatique. Globalement, l'évaluation des techniques a démontré que des modifications manuelles seraient nécessaires si les contours créés par les logiciels devaient être utilisées cliniquement. Les méthodes de segmentation automatique utilisées par les deux produits commerciaux peuvent servir d'excellent point de départ pour le processus de contournage et aussi permettent de réduire la variabilité inter- et intra-médecin lors du contournage.

Dans la deuxième parti, nous avons développé un processus pour l'accumulation de dose en radiothérapie adaptative. En enregistrant les images de planification de la tomodensitométrie (TDM) aux images de tomodensitometrie conique (TDMC), nous avons été en mesure de produire des images modifiées TDMC qui possédait des unités Hounsfield TDM en passant par l'enregistrement déformable des images utilisées. Les distributions de dose ont été recalculées sur les images de TDMC modifiées et ensuite comparées à la distribution de dose prévue. Les résultats indiquent que la cartographie déformable de la densité d'électronique est une technique adéquate pour permettre de recalculer les distributions de dose sur les images de TDMC.

TABLE OF CONTENTS

LIST OF TABLES

LIST OF FIGURES

CHAPTER 1
Introduction

Contents

1.1 Cancer

Cancer is a disease in which a group of cells display uncontrolled reproduction and eventually invade surrounding tissue [20]. Sometimes the cancerous cells spread to other parts of the body via lymph or blood, this is referred to as metastasis. Cancer destroys healthy tissue by competing for resources, this may result in death if left untreated.

According to the Canadian Cancer Society [19], "An estimated 177,800 new cases of cancer (excluding 74,100 non-melanoma skin cancers) and 75,000

deaths from cancer will occur in Canada in 2011." Based on current incidence rates [19], 40% of women and 45% of men in Canada will develop cancer during their lifetimes, one out of every four Canadians are expected to succumb to the disease.

1.2 Cancer Treatments

Once diagnosed, cancer is usually treated with a combination of surgery, chemotherapy and radiation therapy. The choice of treatment depends on multiple factors such as the location, progression of the cancer and the general health of the patient. Surgery is a localized therapy in which the tumor mass is physically removed along with a margin to hopefully include any microscopic disease. Chemotherapy acts by killing cells that divide rapidly, one of the main properties of most cancer cells. The issue with this is that the chemotherapy also harms cells that divide rapidly under normal circumstances: bone marrow cells, hair follicles, digestive tract, etc... Radiation therapy involves the use of ionizing radiation to kill cancer cells. Radiation therapy is in a way much like surgery since they are primarily used to treat well localized cancers.

The aim of radiation therapy is the delivery of a lethal dose to malignant tissues while minimizing the dose to surrounding healthy tissues. Achieving this goal requires precise and accurate localization of the diseased tissues and delivery of the radiation. The fulfillment of the aforementioned requirements has made radiation therapy a distinctly integrated discipline composed of medical imaging and radiation sciences. The following is a list of commonly used radiotherapy treatment modalities,

- External Beam Radiation Therapy (EBRT) [11]
  - Photon Therapy
  - Electron Therapy
  - Proton Therapy

- Brachytherapy [21]

1.3 Imaging in Radiation Therapy

Medical imaging plays a vital role in medicine, especially when used in the diagnosis and treatment of cancer. The images used in radiation therapy are digitally stored in the Digital Imaging and COmmunications in Medicine (DICOM) format. DICOM [2] is a standard for handling, storing, printing, and transmitting information in medical imaging. DICOM files consist of a 3D (or 2D) array of rectangular volume elements, known as voxels, that have defined dimensions and their respective intensities. These files include much more than just the image study, such information ranges from the patient's name and imaging modality to a deformation matrix if applicable. 3D images are often viewed in 2D slices at certain planes, in theory any cross-sectional cut can be viewed but the most common planes are axial, coronal and sagittal. The axial plane divides the body into cranial and caudal (head and tail) portions. The coronal plane divides the body into posterior and anterior (back and front) portions. Finally, the sagittal plane divides the body into sinister and dexter (left and right) portions.

Commonly used imaging modalities in radiation therapy are computed tomography (CT), magnetic resonance imaging (MRI, or simply MR), positron emission tomography (PET) and ultrasound (US). Each modality supplies different information about the disease and the patient. Basic concepts in CT, MR and PET will be discussed in the subsequent subsections.

1.3.1 Computed Tomography

Computed tomography or CT is an imaging modality that produces cross-sectional images representing the X-ray attenuation properties of different tissues. X-rays are produced by an X-ray tube, attenuated by the patient and detected on the other end. This process is repeated until line attenuation measurements have been obtained for all possible angles. From these measurements it is possible to

reconstruct the attenuation at each position of a slice using one of the following algorithms [11]: Filtered backprojection, Fourier transform or series expansion.

Hounsfield developed the first clinical CT scanner [6], it was comprised of one X-ray source and one detector and was capable of producing a slice in five minutes. Presently, CT scanners can acquire upwards of 64 slices per rotation and can reconstruct full 3D volumes in seconds. The output CT image is made up of CT numbers called Hounsfield units, which are based on the attenuation properties of the materials that make up each voxel.

The Hounsfield unit (HU) scale ranges from -1024 to +3072, which is simply a pixel bit-depth of $2^{12} = 4096$ values. The HU number for air and distilled water at standard temperature and pressure are defined as -1000 HU and 0 HU, respectively. Sample HU numbers for various tissues are listed in table 1–1. For a material X with linear attenuation coefficient μ_X, the HU value is given by [3]:

$$\text{HU} = \frac{\mu_X - \mu_{\text{water}}}{\mu_{\text{water}} - \mu_{\text{air}}} \times 1000 \tag{1.1}$$

where μ_{water} and μ_{air} are the linear coefficients of water and air, respectively. A sample CT image is shown in figure 1–1.

Tissue	**HU**
Air	-1000
Lungs	-200
Fat	-120
Water	0
Blood	+30
Muscle	+40
Bone	+400 or more

Table 1–1: Approximate Hounsfield units for various tissues.

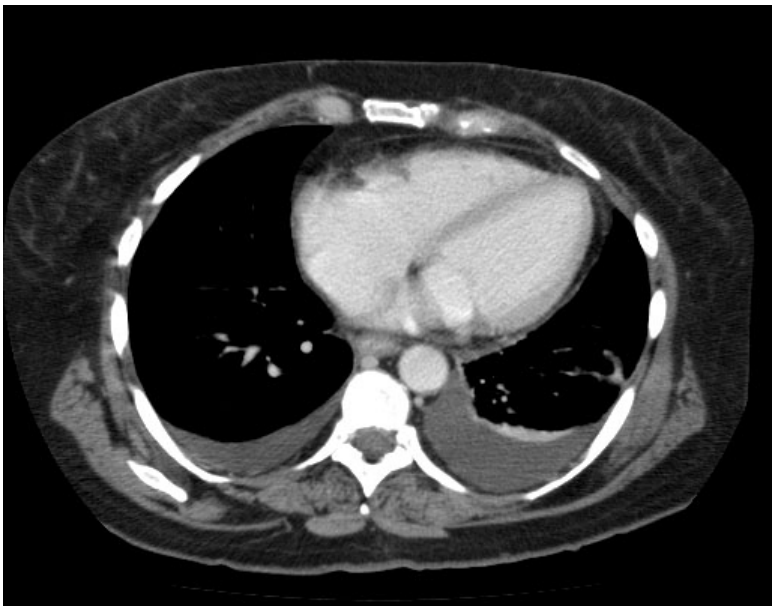

Figure 1–1: Sample axial slices of a 3D CT image. Higher x-ray attenuating objects such as bone are white, while lower attenuating objects such as air are dark.

1.3.1.1 Cone Beam Computed Tomography (CBCT)

The CBCT is a compact version of the regular CT. Through the use of a cone shaped X-ray beam (as opposed to fan-beam for CT), the size of the scanner, radiation dosage and equipment cost are all greatly reduced.

However, the CBCT technology has some substantial drawbacks. kV CBCT images are subject to ample contribution from scatter occurring within the patient and reaching the detector [9]. This effect is more prominent in CBCT than in regular fan-beam CT due to the larger cone angle used and the lack of collimation on the detectors. This scatter contribution degrades the image quality by degrading the contrast. The Hounsfield scale described in section1.3.1 applies to CT scans but not to CBCT scans [22]. A sample CBCT image is shown in figure 1–2.

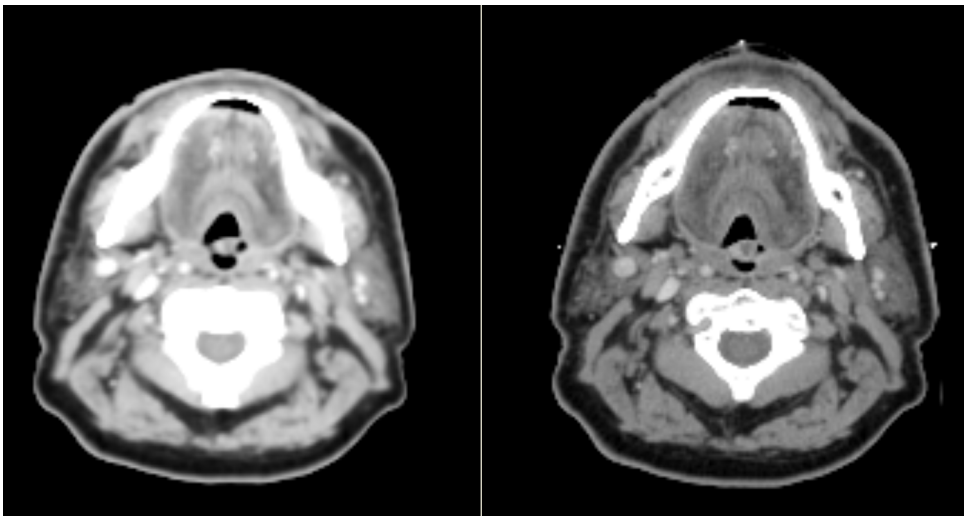

Figure 1–2: Cone beam computed tomography axial image from an on-board imager mounted on a linear accelerator on left. CT image shown on right for comparison.

1.3.2 Magnetic Resonance Imaging

Magnetic resonance imaging (MRI) is based on the concept of nuclear magnetic resonance. The body is largely composed of water molecules, each comprising two hydrogen nuclei. The nucleus of hydrogen and some other atoms have a physical property referred to as magnetic spin. Given a strong, uniform magnetic field, the nuclei will align in the direction of the magnetic field like little magnets; this produces a net magnetization vector. By applying a specific radio frequency pulse the net magnetization vector will tip away from its original orientation, next the net magnetization vector will decay. The rate at which the decay occurs depends on the longitudinal relaxation time (T1) and the transverse relaxation time (T2).

3D MRI images can be generated that depend on T1 or T2. Images whose intensities mainly depend on T1 data are referred to as T1-weighted images, for images dependent on T2 data they are referred to as T2-weighted images. MRI

images have exceptional soft tissue contrast, this is due to the large differences in T1 and T2 values amongst different tissue types, see figure 1–3.

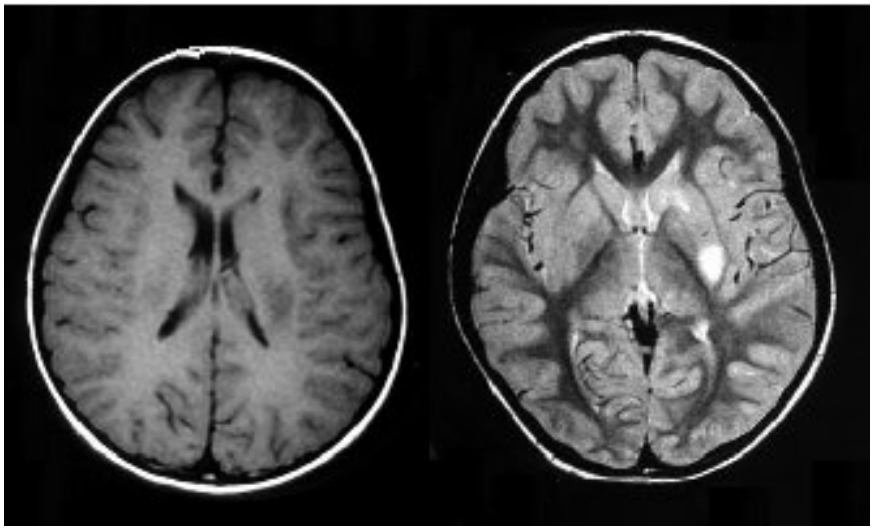

Figure 1–3: T1 (left) and T2 (right) weighted axial MRI images.

1.3.3 Positron Emission Tomography

Radiopharmaceuticals are used in the field of nuclear medicine as tracers in the diagnosis and treatment of many diseases. Positron emission tomography (PET) produces functional 3D images by detecting pairs of gamma rays emitted indirectly by a positron-emitting radiopharmaceutical. The most frequently used radiopharmaceuticals fluorodeoxyglucose (FDG); it is labelled with radioactive fluorine (F-18).

To conduct a scan, the radioactive tracer is injected into the patient, usually intravenously. There is a waiting period for the tracer molecule to become concentrated in tissues of interest. The patient is then placed in the PET scanner. When the F-18 decays, it emits a positron, which when it encounters an electron will annihilate to produce two 511 kilo-electron volt (keV) photons that are emitted at almost 180 degrees to each other. The PET scanner, which consists of many detectors in a ring, now defines a line of response (LOR) by detecting the two 511

keV photons. After detecting the two 511 keV photons, the scanner knows that the event has occurred somewhere along the LOR. After copious amounts of LORs are collected, special image reconstruction methods are employed to obtain the 3D distribution. A sample FDG-PET image is shown in figure 1–4.

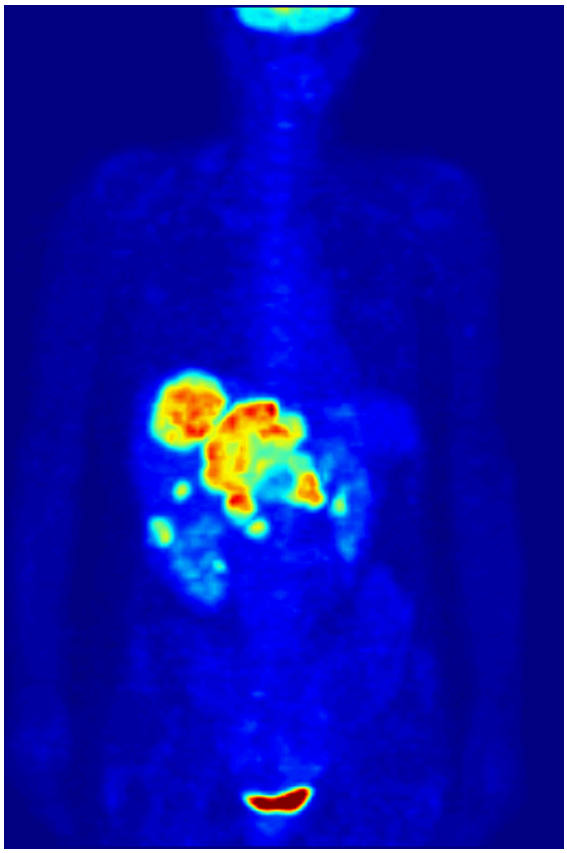

Figure 1–4: Coronal FDG-PET image of a liver metastases of a colorectal tumor case. Note that normal isotope uptake is seen in the brain, renal collection system and bladder.

1.4 Target Volume Definitions

To plan and deliver successful radiation therapy, it is important to accurately define the volumes that must receive tumorcidal doses. The use of common terminology is imperative, since it allows comparisons to be made between therapeutic results after planning and between treatments at different institutions. The International Commission on Radiation Units and Measurements (ICRU) has published several reports used to determine treatment parameters as well as define target volumes so that treatments may be planned and delivered accurately. These reports include ICRU 50 and 62 [14, 15] for photon therapy, ICRU 83 [18] for photon therapy intensity modulated radiotherapy, 71 [16] for electron therapy and 78 [17] for proton therapy. The gross tumor volume (GTV) is defined as: *gross palpable or visible/demonstrable extent and location of malignant growth.* The clinical target volume (CTV) is defined as: *tissue volume that contains a demonstrable GTV and/or subclinical microscopic malignant disease, which has to be eliminated.* The planning target volume (PTV) is defined as: *a volume selecting appropriate beam sizes and beam arrangements, taking into consideration the net effect of all possible geometrical variations, in order to ensure that the prescribed dose is actually absorbed in the CTV.*

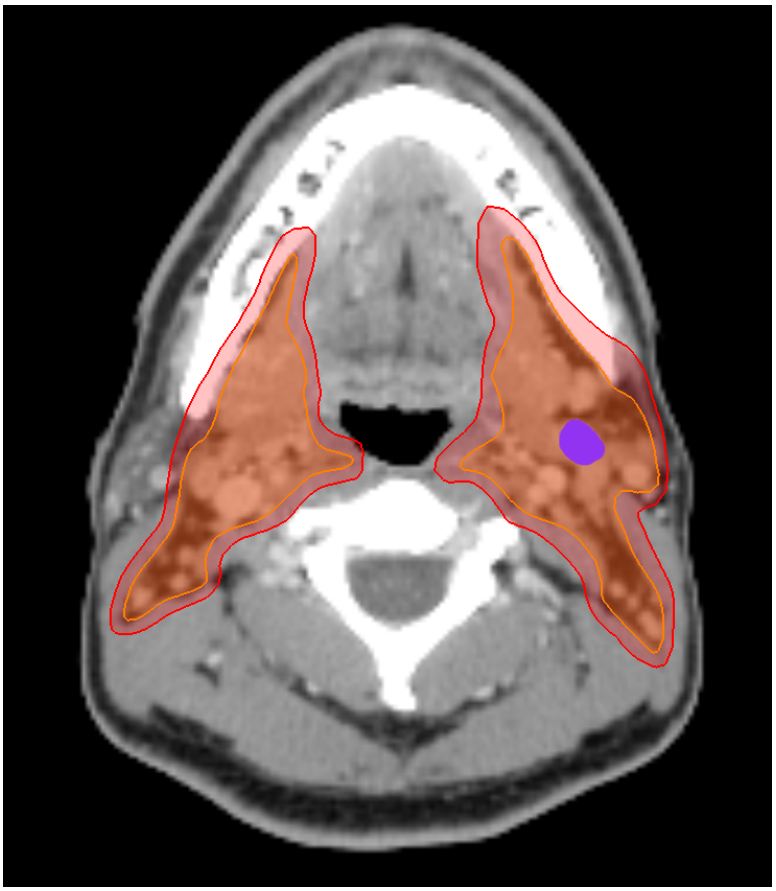

Figure 1–5: Illustration of the boundaries of the volumes defined by report 50 of the International Commission on Radiation Units and Measures (ICRU) on an axial CT image. Gross tumor volume (GTV) is in purple, clinical target volume (CTV) is in orange and planning target volume (PTV) is in red.

Two other volumes of interest are the treated volume (TV) and the irradiated volume (IV). The TV is the volume that has the minimum probability of incurring complications and the IV is the volume that receives a significant dose, based on normal tissue tolerance doses. A representation of the target volume definitions are illustrated in figure 1–5.

1.5 Treatment Planning Process

The treatment planning process consists of target volume and organs at risk (OARs) localization, selection of beam delivery parameters, dose calculation and beam optimization. This is followed by treatment verification and delivery. 3D treatment planning uses CT images taken from a CT-simulator for target volume and OAR delineation and dose calculation. CT-simulators reproduce the same geometry of a treatment unit allowing the images taken from it to be used for treatment planning. MRI-simulators are sometimes used as a complement to CT exist due to their superior soft tissue contrast, dose calculation can only be performed on CT due to its direct connection to electron density which is required for dose calculations [10].

1.5.1 Treatment Plan Evaluation

The aim of radiation therapy is to deliver the maximum possible dose to the tumor volume without exceeding the dose tolerances for healthy tissues. According to the ICRU report 50 [14], the dose delivered to the PTV should be within +7% and -5% of the prescribed dose by the physician. The outcome of the treatment is not only determined by the delivered dose but also the volume of tissue receiving that dose. Treatment plans are commonly evaluated based on isodose distributions, dose statistics and dose volume histograms (DVHs). DVHs present volumetric information about the dose within a particular structure exists in differential and cumulative forms. The differential form is a frequency distribution of the number of voxels which receive a dose within a given dose bin. The cumulative DVH is an integrated form of the differential DVH. Figure 1.5.1 demonstrates typical and ideal cumulative DVHs for target and OARs.

1.5.2 Forward and Inverse Treatment Planning

In conventional forward planning, the user choses the beam configuration based on experience and previous data. The dose distribution is then calculated

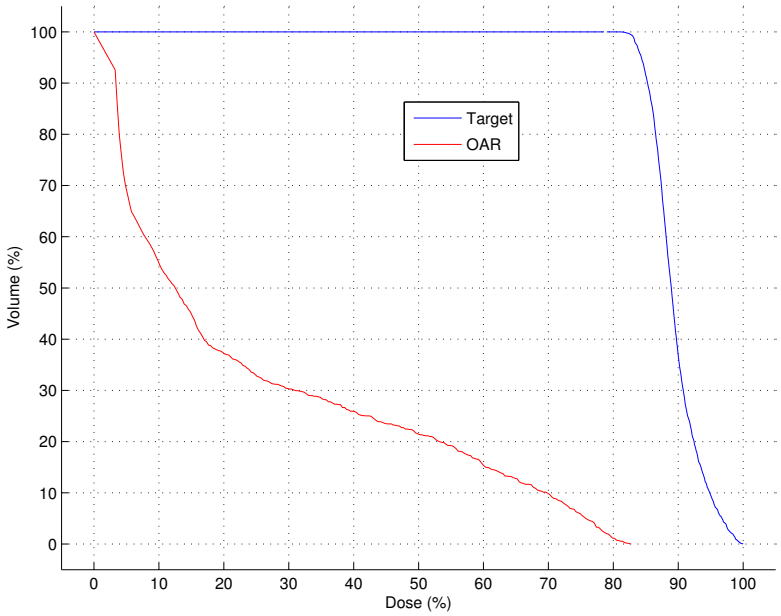

(a) Typical

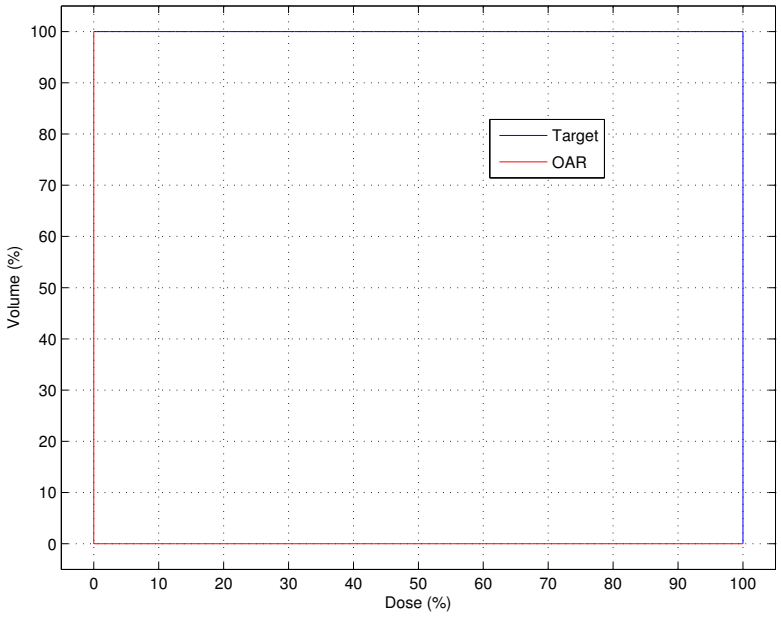

(b) Ideal

Figure 1–6: Sample cumulative dose volume histograms for a target and organ at risk for the typical case (a) and the ideal case (b).

and modifications to the plans may be executed to improve the dose distribution. Complicated dose distributions such as those produced by intensity modulated radiation therapy (IMRT) are usually produced using an inverse treatment

planning process. In inverse planning, the user specifies a set of criteria for the dose delivery to the target and select OARs. The treatment planning software uses the user-defined criteria to find the optimized intensity which minimizes a cost function [23], this process is achieved using an iterative algorithm.

1.6 Advanced Radiotherapy Protocols

1.6.1 Intensity Modulated Radiotherapy

IMRT is a three-dimensional radiotherapy technique that yields dose distributions which are highly conformal to the tumor target while sparing surrounding healthy tissue. IMRT, as the name suggests, uses beams with non-uniform intensity. There are multiple ways of achieving this, namely: multi-leaf collimators (MLCs), scanned beams [7], physical compensators or modulated fan beam (Tomotherapy). The most common method of achieving a non-uniform beam is with the use of the MLCs. The MLC techniques deliver an intensity modulated field by either moving the collimator leaves during irradiation or by irradiating a sequence of static MLC configurations. The former is often referred to as the dynamic MLC technique and the latter as the step-and-shoot MLC technique [4].

1.6.2 Image Guided Radiotherapy (IGRT)

The proper positioning of the patient is crucial to achieve optimal treatment delivery, especially with IMRT due to the high dose gradients. IGRT is an advanced radiotherapy technique that adopts imaging technology to guide the localization of the radiation target throughout the course of treatment. Daily or weekly alignment imaging is common practice in modern radiotherapy [13]. Without the use of IGRT the PTV margin is larger to compensate for localization errors during treatment [8]. By improving precision and accuracy through IGRT, the PTV margin may be reduced relative to non-IGRT treatments, resulting in a reduction of the amount of radiation delivered to healthy normal tissue. Cone beam computed tomography (CBCT) and 2D kV radiographs are commonly used

in IGRT techniques. See figure 1–7 for a photo of the on-board imaging (OBI) device which allows CBCT images and kV radiographs to be acquired from Varian's Trilogy linac (Varian Medical Systems, Inc., Palo Alto, California).

Figure 1–7: Photograph of a Varian Triology (Varian Medical Systems, Inc., Palo Alto, California) linac with the on-board imaging device extended on the sides.

IGRT has much evolved in the last decade with the incorporation of CT scanners into radiotherapy treatment rooms [8]. These include OBI devices, CT scanners mounted on linacs (CT-on-Rails) as well as the HI*Art II helical on Tomotherapy system. By acquiring a 3D image of the patient in the treatment position, image registration can be performed to apply the required shift to map the treatment CT to the original planning CT. IGRT significantly increases the chance that the target volume receives the prescribed dose, yet its drawback is in its inability to compare the planned and delivered doses to the target volumes and OARs. This issue provides the basis for adaptive radiation therapy.

1.6.3 Adaptive Radiation Therapy (ART)

ART utilizes daily imaging (usually CT or CBCT) to track anatomical changes such as displacement and deformation of the target volumes and/or OARs, subsequently the treatment plan is adapted for the following treatment. The ART process which combines image guidance, deformable image registration, dose reconstruction, dose calculation and plan re-optimization to compensate for uncertainties in inter-fraction setup and organ deformation.

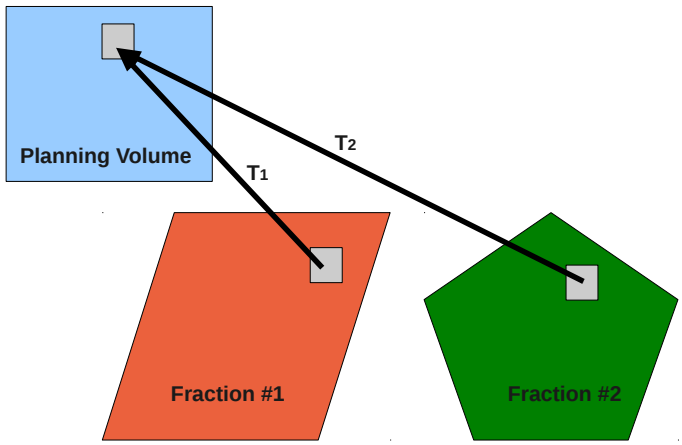

Figure 1–8: Diagram demonstrating dose summation by determining the mapping between the treatment plan CT image and the daily treatment CT images.

It has been shown that by applying the daily treatment CT images to the treatment plan CT, the delivered dose distribution for each fraction can be precisely calculated [12, 24]. By applying deformable image registration, the dose delivered to each voxel of tissue in the planning CT image can be tracked and accumulated over the course of treatment. This approach is referred to as dose accumulation [1, 5] and is illustrated in figure 1–8. If at any point during the course of the treatment the accumulated dose to the OARs is too high and/or

the accumulated dose to the target volume is too low, the treatment plan may be modified.

References

[1] Schaly B, Kempe JA, Bauman GS, Battista JJ, and Van Dyk J. Tracking the dose distribution in radiation therapy by accounting for variable anatomy. *Phys Med Biol*, 49, 2004.

[2] WD Bidgood and SC Horii. "introduction to the acr-nema dicom standard". *Radiographics*, 12, 1992.

[3] Rodney A. Brooks. A quantitative theory of the hounsfield unit and its application to dual energy scanning. *Journal of Computer Assisted Tomography*, 1, 1977.

[4] Sha X. Chang, Timothy J. Cullip, and Katharin M. Deschesne. Intensity modulation delivery techniques: "Step & shoot" mlc auto-sequence versus the use of a modulator. *Medical Physics*, 27, 2000.

[5] Yan D, Jaffray DA, and Wong JW. A model to accumulate fractionated dose in a deforming organ. *Int J Radiat Oncol Biol Phys*, 44, 1999.

[6] Hounsfield G.N. Computerized transverse axial scanning (tomography): Part 1. description of system. *British J Radiology*, 46, 1973.

[7] Intensity Modulated Radiation Therapy Collaborative Working Group. Intensity-modulated radiotherapy: current status and issues of interest. *Int J Radiat Oncol Biol Phys*, 4, 2001.

[8] Jaffray DA, Bissonnette JP, Craig T. *X-ray Imaging for Verification and Localization in Radiation Therapy in Modern Technology of Radiation Oncology (suppl. 1). Modern Technology of Radiation Oncology.* Medical Physics Publishing, 1999.

[9] Geneviève Jarry, Sean A. Graham, Douglas J. Moseley, David J. Jaffray, Jeffrey H. Siewerdsen, and Frank Verhaegen. Characterization of scattered radiation in kv cbct images using monte carlo simulations. *Medical Physics*, 33, 2006.

[10] Joakim Jonsson, Magnus Karlsson, Mikael Karlsson, and Tufve Nyholm. Treatment planning using mri data: an analysis of the dose calculation accuracy for different treatment regions. *Radiation Oncology*, 5, 2010.

[11] Faiz M. Khan. *The Physics of Radiotherapy.* Lippincott Williams & Wilkins, third edition, 2003.

[12] Langen KM, Meeks SL, Poole DO, Wagner TH, Willoughby TR, Kupelian PA, Ruchala KJ, Haimerl J, and Olivera GH. The use of megavoltage ct (mvct) images for dose recomputations. *Phys Med Biol*, 50, 2005.

[13] Jasper Nijkamp, Floris J. Pos, Tonnis T. Nuver, Rianne de Jong, Peter Remeijer, Jan-Jakob Sonke, and Joos V. Lebesque. Adaptive radiotherapy for prostate cancer using kilovoltage cone-beam computed tomography: First clinical results. *Radiotherapy and oncology : journal of the European Society for Therapeutic Radiology and Oncology*, 70, 2008.

[14] International Commission on Radiation Units and Measurements. ICRU Report 50: Prescribing, recording, and reporting photon beam therapy. *International Commission on Radiation Units and Measurements*, 1993.

[15] International Commission on Radiation Units and Measurements. ICRU Report 62: Prescribing, recording and reporting photon beam therapy (supplement to icru report 50). *International Commission on Radiation Units and Measurements*, 1999.

[16] International Commission on Radiation Units and Measurements. ICRU Report 71: Prescribing, recording, and reporting electron beam therapy. *International Commission on Radiation Units and Measurements*, 2004.

[17] International Commission on Radiation Units and Measurements. ICRU Report 78: Prescribing, recording, and reporting proton beam therapy. *International Commission on Radiation Units and Measurements*, 2007.

[18] International Commission on Radiation Units and Measurements. ICRU Report 83: Prescribing, recording, and reporting photon-beam intensity-modulated radiation therapy (imrt). *International Commission on Radiation Units and Measurements*, 2007.

[19] Canadian Cancer Society. Cancer canada statistics. *http://www.cancer.ca/Canada-wide/About%20cancer/Cancer%20statistics.aspx?sc_lang = en*, 2011.

[20] Canadian Cancer Society. Cancer canada: Types of cancer. *http://www.cancer.ca/Canada-wide/About%20cancer/Types%20of%20cancer.aspx?sc_lang = en*, 2011.

[21] T Vuong, Slobodan Devic, Belal Moftah, Michael Evans, and Ervin B. Podgorsak. High-dose-rate endorectal brachytherapy in the treatment of locally advanced rectal carcinoma: Technical aspects. *Brachytherapy*, 4, 2005.

[22] G.R.J. Swennen W. De Vos, J. Casselman. Cone-beam computerized tomography (cbct) imaging of the oral and maxillofacial region: A systematic review of the literature. *International journal of oral and maxillofacial surgery*, 38, 2009.

[23] S Webb. The physical basis of imrt and inverse planning. *British Journal of Radiology*, 76, 2003.

[24] Yong Yang, Eduard Schreibmann, Tianfang Li, Chuang Wang, and Lei Xing. Evaluation of on-board kv cone beam ct (cbct)-based dose calculation. *Physics in Medicine and Biology*, 52, 2007.

CHAPTER 2
Concepts in Deformable Image Registration and its Applications

Contents

2.1 Medical Image Registration

2.1.1 Definition

Image registration is the process of transforming different images (or image sets) into one coordinate system. It is a method for determining the similarity of features between images collected at different times or using different imaging modalities. The similarity is then used to to transform one image so it closely resembles the other so that the pair of images can be directly analyzed. A common use of registration is to correct for different patient positions between scans. Image registration adds value to images by allowing structural (CT, MR, US) and functional (PET, SPECT, fMRI) images to be studied in the same coordinate system and can allow disease progression to be monitored over time. Registration of images from different modalities is known as inter-modality registration and

intra-modality registration is the registration of images acquired from the same imaging modality. Image registration is also classified as either rigid or deformable (non-rigid). Rigid registration involves only translation and rotation (six degrees of freedom) whereas deformable or non-rigid registration takes into account deformable anatomical or biological changes between images.

2.1.2 Notation

Image registration determines the mapping between two images, F (floating) and R (target), spatially with respect to intensity [3]. The mapping between images can be expressed as:

$$R = T(F) \tag{2.1}$$

where T is the spatial transformation. For 3D images, T simply maps three spatial coordinates, x_F, y_F and z_F, to new spatial coordinates, x_R, y_R and z_R. The transformation T is defined over a finite domain which can consist of the entire images or just a section, this finite domain is referred to as a mask. Figure 2–1 illustrates the concept of spatial transformation T that maps from arbitrary point A in one image to point B in the second image.

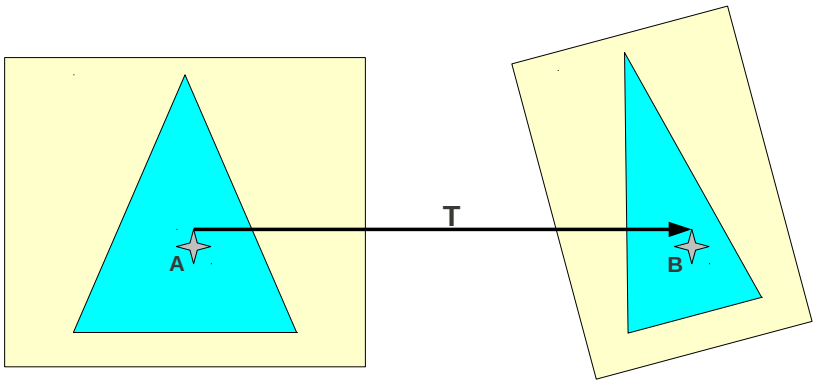

Figure 2–1: Image registration determines a spatial transform that maps one image onto another.

2.1.3 Workflow

When registering two images, one is taken as the floating image F, and the other as the target image R. The objective of registration is to find the optimal mapping that will align image F to R. Components of the registration workflow include the transformation, interpolator and similarity measure (cost function). Figure 2–2 illustrates a sample registration workflow.

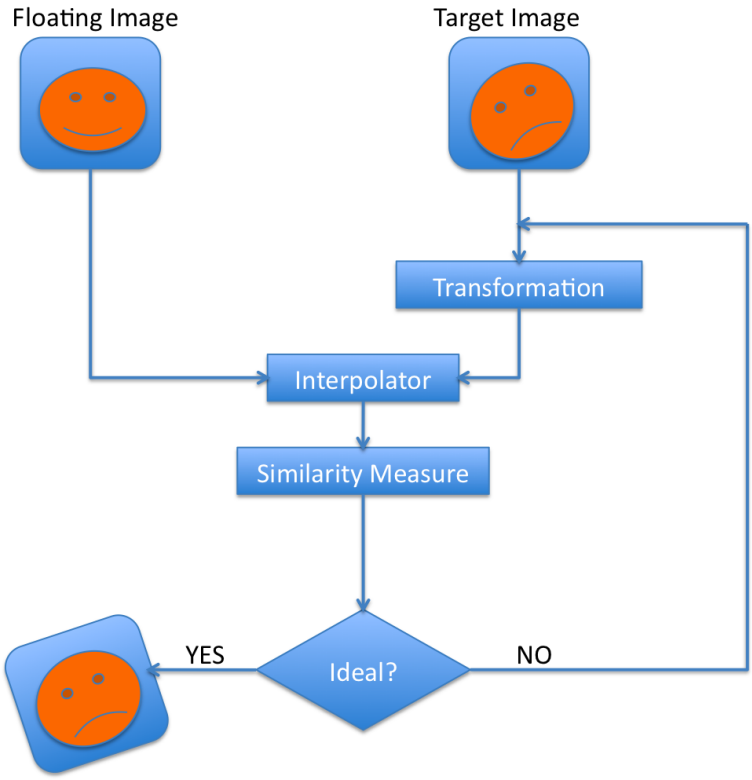

Figure 2–2: Sample image registration workflow. The output is the floating image registered to the target image.

The interpolator is used to determine the intensity values at certain points when images are moved. The similarity measure is used to calculate how well two images match, this is the cost function.

2.1.4 Transformations

Transformations between floating and target images can be either rigid (translation and rotation only) or deformable. The rigid transformation is a transformation that preserves distances between pairs of points; objects will have the same shape and size after a rigid transformation. A rigid transformation

is defined as a transformation, which when acting on a vector v, produces a transformed vector $T(v)$ expressed as:

$$T(\mathbf{v}) = R\mathbf{v} + \mathbf{t} \tag{2.2}$$

where R is a rotation and $\mathbf{t}$ is a translation vector [6]. The rigid transformation is described by six degrees of freedom, which is useful for many medical applications but is often insufficient to describe without warping the floating image to describe the target image.

The simplest form of the deformable transformation is the affine transform, which is an extension of the rigid transform where scaling and shearing are permitted [8]. This transform is described by twelve degrees of freedom in the first order polynomials transformation, second, third and fourth order polynomial transformations yield a total of 30, 60 and 105 degrees of freedom, respectively. The affine transformation is limited in that it can only model global deformations and not local ones, which is more applicable to realistic medical applications. A common approach is the use of freeform deformations (FFD) [5] based on locally controlled functions. A very common locally controlled function is the B-splines [5], which are defined by a mesh of control points with uniform spacing δ. In this method, the control point $\phi_{i,j,k}$ is moved around and the floating image is deformed by:

$$T^{\text{B-Splines}} = \sum_{l=0}^{3}\sum_{m=0}^{3}\sum_{n=0}^{3} B_l(u)B_m(v)Bn(w)\phi_{i+l,j+m,k+n} \tag{2.3}$$

where $i = \lfloor \frac{x}{n_x} \rfloor - 1$, $j = \lfloor \frac{y}{n_y} \rfloor - 1$, $k = \lfloor \frac{z}{n_z} \rfloor - 1$, $u = \frac{x}{n_x} - \lfloor \frac{x}{n_x} \rfloor$, $v = \frac{y}{n_y} - \lfloor \frac{y}{n_y} \rfloor$, $w = \frac{z}{n_z} - \lfloor \frac{z}{n_z} \rfloor$ and B_l represents the lth basis function of the B-spline:

$$\begin{aligned} B_0(u) &= \frac{(1-u)^3}{6} \\ B_1(u) &= \frac{(3u^3 - 6u^2 + 4)}{6} \end{aligned}$$

$$B_2(u) = \frac{-3u^3 + 3u^2 + 3u + 1}{6}$$
$$B_3(u) = \frac{u^3}{6}$$

As previously mentioned, the B-spline are locally controlled, which means that changing the location of one control point affects the transformation of the local neighborhood of that control point only. Computationally, the B-splines is efficient even for a large number of control points.

Another class of deformable registration algorithms are non-parametric transforms where the transformation is defined by a discrete set of displacement vectors instead of a continuous function. The main advantage to using non-parametric deformable transformations is that there is a considerable increase in freedom when modeling large local deformations.

2.1.5 Similarity Measures

Similarity measures are a metric of how well two images match. Image registration algorithms find the transformation that optimizes the similarity measure (cost function). Conceptually, the simplest similarity measure is the sum of intensity differences between each pair of voxels. The ideal case is when the sum is zero, which would imply that the two images are perfectly aligned. A commonly used similarity metric based on difference in intensity is the sum of squared differences (SSD), which is calculated as follows:

$$\text{SSD} = \frac{1}{N}\sum_{X}(T(x) - F(t(x)))^2 \tag{2.4}$$

where $T(x)$ is the intensity at a position x in an image (target) and F(t(x)) is the intensity at the corresponding point (in the floating image) given by the current estimate of the transformation t(x). N is the number of voxels. This type of similarity metrics are appropriate for images that differ only by Gaussian noise [1],

there are sensitive to small number of voxels that have very large intensity differences and are only applicable to mono-modal image registration. Similarity measures based on correlation between images are also quite common. The correlation coefficient (CC) is one of the more used correlation-based metrix and defined as:

$$\mathrm{CC} = \frac{\sum_X (T(x) - \bar{T}) \cdot (F(t(x)) - \bar{F})}{\sqrt{\sum_X (T(x) - \bar{T})^2 \sum_X (F(t(x)) - \bar{F})^2}}, \tag{2.5}$$

CC is also based on voxel intensities and is only suitable for mono-modal images.

A different class of similarity measure is required for voxel-based inter-modality registration, a commonly used similarity metric for this problem is mutual information (MI) [4]. MI is derived from an information-theoretic approach to the dependence of on variable on another; it assumes that only a probabilistic relationship between intensities exists. It is based on the shared information between overlapping regions of two images, which should be maximized at registration. MI is defined in terms of entropies of the intensity distribution as follows:

$$\mathrm{MI} = H_\mathrm{T} + H_\mathrm{S} - H_\mathrm{TS} \tag{2.6}$$

with

$$\begin{aligned} H_\mathrm{T} &= -\sum_i P_i \log P_i, \\ H_\mathrm{S} &= -\sum_j Q_j \log Q_j \text{ and} \\ H_\mathrm{TS} &= -\sum_{i,j} p_{i,j} \log p_{i,j} \end{aligned}$$

where P (or Q) is the probability of intensity I (or J) occurring in the target (or floating) image and $p_{i,j}$ is the joint probability of both occurring at the same place.

2.2 Atlas

IMRT is driven by volumetric segmentation, which necessitates greater care and accuracy when contouring OARs and target volumes. The anatomical contouring process requires both clinical knowledge and a significant workload. Atlas-based anatomical segmentation can be used to automatically obtain contours of a patient scan. The previously described image registration methods are applied to atlas-based image segmentation, figure 2–3 illustrates the basic framework for atlas-based segmentation. A pre-labeled image, known as the atlas, is first registered using a deformable algorithm to the subject image to be segmented. The deformation field used to register the atlas to the subject image is extracted and then applied to the atlas mask[1] . The transformed structures delineated in the atlas are projected onto the subject image. The output is the segmented subject image.

[1] A mask is a binary image, in this context each structure in the atlas has a mask which is deformed and subsequently projected onto the subject image.

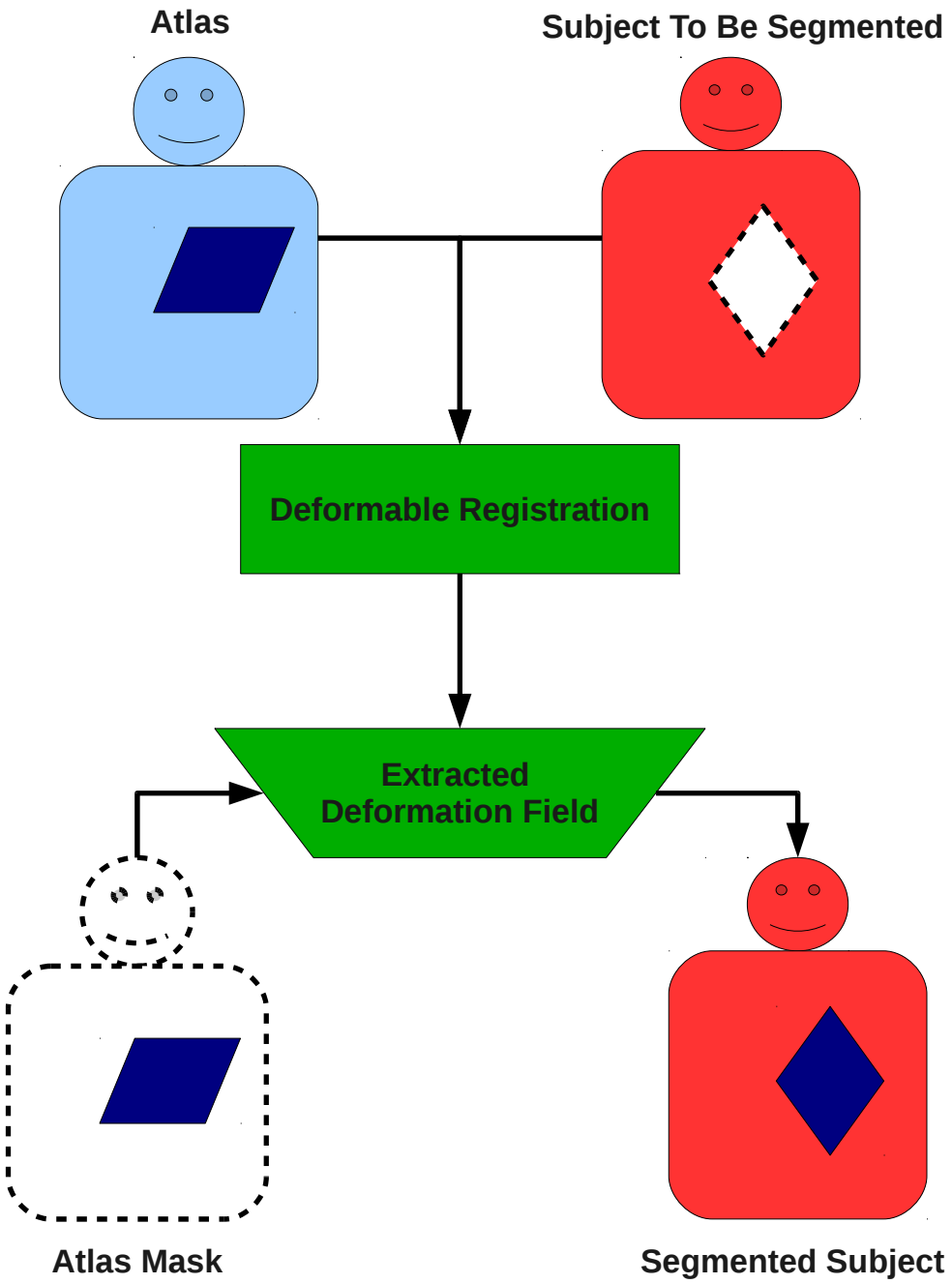

Figure 2–3: A simple framework for atlas-based segmentation. The atlas is first registered to the subject image using deformable registration. The deformation field is extracted and applied to the structures from the atlas, which maps the structures onto the subject image.

Atlases in this work were created using in-software tools (see section 2.4). Atlases were created using a set of patient data sets, which included the planning CT image and the physician-drawn contours.

2.2.1 STAPLE Algorithm

The Simultaneous Truth and Performance Level Estimation (STAPLE) algorithm is a widely accepted tool that adjusts for inter- and intra-expert variability in image segmentation [7]. It takes in a collection segmentations and calculates a probabilistic estimate of the true segmentation. Using this algorithm, we took a collection of structure sets (single-patient-based atlases) and generated an estimate of the true segmentation; an average atlas was created.

2.2.2 Validation

To evaluate the performance of the atlas-based segmentation, we compared the atlas-based contours to expert-drawn contours. For the segmentation performance evaluation, the Dice Similarity Coefficient (DSC) metric was computed [2]. For two contours with volumes V_1 and V_2, the DSC is defined as the ratio of the volume of their intersection to their average volume:

$$\text{DSC} = 2\frac{V_1 \bigcap V_2}{V_1 + V_2} \tag{2.7}$$

where the DSC has a value of 1 for perfect agreement and 0 when the structures do not overlap.

2.3 Deformable Contour Propagation

The idea behind deformable contour propagation is very much similar to atlas-based segmentation except that in deformable contour propagation the segmentation is based on only one patient data set. This could be more powerful than using a multi-patient-based atlas when propagating contours for a given patient. An example of this would be when propagating contours from a planning CT to a weekly CBCT or when a patient requires a new planning CT due to

weight loss; the original planning CT would be registered to the new scan, then the extracted deformation field would be applied to the original planning CT's structure set.

2.4 Software Packages

Two commercially available deformable medical image registration software packages were used in this research. VelocityAI version 2.4 (Velocity Medical Solutions, Atlanta, GA) and MIMvista version 5 (MIM; MIMvista, Cleveland, OH) were both run on a 3.2 GHz iMac (Apple, Cupertino, California) with 1 TB of hard disk space. Both deformable registration tools were used to create atlases using archived patient data, non-rigidly register image sets and automatically segment patient images using atlas-based segmentation and deformable contour propagation.

References

[1] W R Crum. Non-rigid image registration: theory and practice. *British Journal of Radiology*, 77, 2004.

[2] Lee R. Dice. Measures of the amount of ecologic association between species. *Ecology*, 26, 1945.

[3] L Gottesfeld Brown. A survey of image registration techniques. *ACM Computing Surveys CSUR*, 24, 1992.

[4] Josien P W Pluim, J B Antoine Maintz, and Max a Viergever. Mutual-information-based registration of medical images: a survey. *IEEE transactions on medical imaging*, 22, 2003.

[5] D Rueckert, L I Sonoda, C Hayes, D L Hill, M O Leach, and D J Hawkes. Nonrigid registration using free-form deformations: application to breast MR images. *IEEE transactions on medical imaging*, 18, 1999.

[6] Ana Irene Ramrez Galarza & José Seade. *Introduction to classical geometries*. Birkhauser, 2007.

[7] Simon K Warfield, Kelly H Zou, and William M Wells. Simultaneous truth and performance level estimation (STAPLE): an algorithm for the validation of image segmentation. *IEEE transactions on medical imaging*, 23, 2004.

[8] B Zitova. Image registration methods: a survey. *Image and Vision Computing*, 21, 2003.

CHAPTER 3
Evaluation of Atlas-Based Segmentation and Deformable Contour Propagation

Contents

3.1 Introduction

The quality of contours in treatment plans plays an important role in radiation therapy. Images from various imaging modalities provide increasing information of healthy and malignant tissues of a subject. Automatic image segmentation techniques used for the delineation of anatomical structures and others regions of interest are becoming increasingly important in facilitating quantification of tissue volumes, study of anatomical structures and treatment planning [1].

Intensity modulated radiation therapy (IMRT) is designed to be highly conformal to the three-dimensional shape of a tumor volume, which yields a dose distribution that maximizes the dose to the tumor while sparing healthy normal

tissue. There may also be an increased risk that the high degree of conformality will lead to steep dose gradients, which inturn increase the risk of a geometrical miss, especially for sites where positioning and organ motion are more uncertain. IMRT is driven by volumetric segmentation, thus the contours for the organs at risk (OAR) and the target volumes must be meticulous. This increase in care comes at the cost of valuable physician and dosimetrist time. We have thus evaluated the atlas-based segmentation and deformable contour propagation techniques presented in Chapter 2.

3.2 Methods and Materials

3.2.1 Atlas-Based Segmentation

VelocityAI and MIMvista were compared. Twenty-one IMRT head and neck (HN) cases were randomly and retrospectively chosen. These cases included their respective planning CT scans and physician-drawn structures. The twenty-one cases were divided into two sets: one to create the atlas (eleven) and the other to test the atlas on (ten). In MIMvista, the atlas was created using the in-software tool and setting the most representative patient as the atlas template. In VelocityAI, the atlas was created using all ten cases to create an average patient atlas. The STAPLE algorithm was used to take collections of single-patient-based atlases to calculate a probabilistic average atlas for the VelocityAI method. The atlas-based contours were compared to physician-drawn contours using DSC.

3.2.1.1 Patient Data Requirements

The twenty-one IMRT HN cases used for the atlas-based segmentation method were chosen such that all twenty-one patients had twelve specific OARs already contoured. Each patient was treated with roughly the same degree of neck extension.

3.2.2 Deformable Contour Propagation

Eleven HN and sixteen gynecologic (GYN) brachytherapy cases were randomly and retrospectively chosen for this study. These cases included their respective pre-treatment (pCT) and follow-up CT (fCT) scans along with their respective physician-drawn structures. The pCT volume was registered using VelocityAI's deformable algorithm to the fCT and the resulting deformation field was applied to the pCT's structure set to propagate it to the fCT. The propagated contours were compared to physician-drawn contours using the DSC.

3.2.2.1 Patient Data Requirements

The eleven HN cases used for deformable contour propagation were re-scanned and re-contoured at least once. All HN cases had twelve specific structures in common. The sixteen GYN brachytherapy cases were all treated using the Miami applicator [2] and all had three CT scans.

3.3 Results and Discussion

3.3.1 Atlas-Based Segmentation

Ten OARs were automatically segmented using VelocityAI and MIMvista and were compared to the physician-drawn contours using the DSC as seen in table 3–2. VelocityAI and MIMvista performed quite well with the brain, cord and eyes with mean DSC values ranging between 0.68-0.95 and 0.75-0.98 respectively. The spinal cord DSC values are not representative due to the fact that physicians may not always contour the entire structure. VelocityAI outperformed MIMvista for the brainstem, with a mean DSC of 0.77 ± 0.06 versus 0.7 ± 0.1 for MIMvista. MIMvista yielded better results for the mandible, with a mean DSC of 0.8 ± 0.2 versus 0.6 ± 0.1 for VelocityAI. Both had some trouble with the oral cavity, parotids and sphincter muscle with DSCs ranging between 0.41-0.69 for VelocityAI and 0.38-0.71 for MIMvista. It should be noted that the physician-drawn contours are

taken as the gold standard. A way to improve this study would be to have multiple physicians contour all the structures and then create a probabilistic average using the STAPLE algorithm, this average would then be used as the gold standard when evaluating the automatically segmented structures.

Abbreviation	**Expansion**
BrnStm	Brain Stem
Esoph	Esophagus
Lrynx	Larynx
Mndbl	Mandible
OrlCvT	Oral Cavity
Paro	Parotid

Table 3–1: Expansions for the abbreviations found in tables 3–3 and 3–2.

	Brain		BrnStm		Cord		Eye-L		Eye-R		Mndbl		OrlCvT		Paro-L		Paro-R		Sphincter		Mean (STD)	
Pt#	**V**	**M**	**V**	**M**	**V**	**M**	**V**	**M**	**V**	**M**	**V**	**M**	**V**	**M**	**V**	**M**	**V**	**M**	**V**	**M**	**V**	**M**
ABS01	0.94	0.98	0.78	0.70	0.24	0.33	0.78	0.72	0.77	0.84	0.25	0.23	0.27	0.11	0.64	0.66	0.66	0.62	–	–	0.59 (0.27)	0.58 (0.29)
ABS02	0.94	0.97	0.78	0.51	0.76	0.78	0.78	0.82	0.81	0.83	0.74	0.87	0.50	0.43	0.62	0.76	0.60	0.74	0.32	0.54	0.68 (0.18)	0.73 (0.18)
ABS03	–	–	0.77	0.78	0.71	0.89	0.83	0.89	0.84	0.90	0.70	0.87	0.65	0.74	0.65	0.80	0.71	0.76	0.50	0.00	0.71 (0.10)	0.74 (0.28)
ABS04	0.96	0.98	0.65	0.64	0.74	0.87	0.81	0.65	0.75	0.70	0.64	0.80	0.51	0.21	0.81	0.81	0.72	0.73	0.33	0.24	0.69 (0.17)	0.67 (0.25)
ABS05	0.95	0.97	0.83	0.73	0.80	0.79	0.72	0.84	0.74	0.79	0.59	0.84	0.57	0.56	0.65	0.72	0.61	0.52	0.28	0.48	0.67 (0.18)	0.72 (0.16)
ABS06	–	–	0.72	0.72	0.80	0.72	0.90	0.84	0.87	0.87	0.60	0.79	0.43	0.13	0.42	0.69	0.68	0.69	0.37	0.17	0.64 (0.20)	0.62 (0.28)
ABS07	0.95	0.98	0.80	0.60	0.77	0.79	0.80	0.78	0.73	0.76	0.64	0.83	0.57	0.64	0.74	0.55	0.70	0.36	0.43	0.43	0.71 (0.14)	0.67 (0.19)
ABS08	0.95	0.98	0.84	0.59	0.62	0.77	0.79	0.81	0.76	0.81	0.61	0.85	0.51	0.04	0.71	0.65	0.75	0.65	0.48	0.55	0.70 (0.15)	0.67 (0.26)
ABS09	0.93	0.98	0.72	0.62	0.66	0.74	0.74	0.70	0.68	0.67	0.58	0.75	0.62	0.31	0.60	0.73	0.69	0.76	0.32	0.35	0.65 (0.16)	0.66 (0.20)
ABS10	0.96	0.98	0.83	0.86	0.68	0.86	0.85	0.92	0.82	0.92	0.73	0.87	0.75	0.72	–	–	0.79	0.75	0.64	0.64	0.78 (0.10)	0.84 (0.11)
Mean	0.95	0.98	0.77	0.67	0.68	0.75	0.80	0.80	0.78	0.81	0.61	0.77	0.54	0.39	0.65	0.71	0.69	0.66	0.41	0.38		
STD	0.01	0.01	0.06	0.10	0.17	0.16	0.05	0.08	0.06	0.08	0.14	0.19	0.13	0.26	0.11	0.08	0.06	0.13	0.12	0.21		

Table 3–2: DSC values for various structures for the head and neck cases using the atlas-based segmentation method. The cells are red for DSC values from 0-0.7, yellow till 0.8 and green till unity. VelocityAI and MIMvista are denoted by **V** and **M**, respectively. The spinal cord DSC values are not representative due to the fact that physicians may not always contour the entire structure. Abbreviations of structures are expanded in table 3–1.

We also evaluated the performance of VelocityAI and MIMvista on the 11 patients that were used to create the atlas. The overall average DSC values for VelocityAI and MIMvista were 0.7 ± 0.2 and 0.93 ± 0.04 respectively. MIMvista outperforms VelocityAI here due to the nature of its algorithm. MIMvista will search for the best matching patient from its atlas database and use it as the reference, hence why MIMvista fares better when using patients, which are part of the atlas. VelocityAI did not achieve a perfect segmentation since the patients' structure sets were averaged using the STAPLE algorithm.

3.3.2 Deformable Contour Propagation

Eleven OARs and two CTVs were analyzed for the HN cases, as well as the Miami applicator, bladder, rectum and CTV for the GYN cases. The propagated contours obtained from deformable contour propagation were compared to physician-drawn contours using the DSC metric. DSC values for the HN and GYN cases are summarized in table 3–3 and table 3–4, respectively. As discussed in section 3.3.1, the study could be improved in the future by having multiple physicians contour all the structures and creating a probabilistic average using the STAPLE algorithm, this average would then be used as the gold standard when evaluating the automatically segmented structures.

Pt#	Brain	BrnStm	Cord	Esoph	Eye-L	Eye-R	Lrynx	Mndbl	OrlCvT	Paro-L	Paro-R	CTV1	CTV2	Mean	STD
HN01	0.98	0.80	0.81	0.72	0.81	0.83	0.77	0.77	0.84		0.73			0.81	0.07
HN02	0.98	0.91	0.87	0.77	0.92	0.92	0.73	0.91	0.89	0.87	0.85	0.86		0.87	0.07
HN03	0.97	0.89	0.82		0.87	0.87	0.91	0.83	0.87	0.88	0.83	0.90	0.82	0.87	0.04
HN04		0.87	0.90	0.83	0.90	0.93	0.85	0.88	0.81	0.78	0.84	0.89	0.87	0.86	0.04
HN05	0.98	0.87	0.75	0.75	0.86	0.90	0.81	0.77			0.67	0.85	0.75	0.81	0.09
HN06	0.98	0.76	0.69	0.55	0.93	0.85	0.71	0.87			0.75	0.88	0.51	0.77	0.15
HN07	0.97	0.87	0.87		0.90	0.88	0.70	0.87	0.79	0.72	0.78	0.90	0.78	0.83	0.08
HN08	0.98	0.74	0.78	0.65	0.90	0.83		0.84	0.67	0.82	0.80	0.86	0.85	0.81	0.09
HN09	0.97	0.82	0.69	0.40	0.89	0.88	0.81	0.83	0.73	0.81	0.84			0.79	0.15
HN10	0.97	0.86	0.69	0.36	0.83	0.85	0.73	0.83	0.46	0.81	0.74	0.90	0.40	0.72	0.20
HN11	0.98	0.87	0.79	0.69	0.87	0.89	0.88	0.87	0.37	0.73	0.74	0.82	0.84	0.79	0.15
Mean	0.98	0.84	0.79	0.64	0.88	0.88	0.79	0.84	0.71	0.80	0.78	0.87	0.73		
STD	0.01	0.05	0.08	0.16	0.04	0.03	0.07	0.05	0.18	0.06	0.06	0.03	0.18		

Table 3–3: DSC values for various structures for the head and neck cases using the deformable contour propagation method (VelocityAI only). The cells are red for DSC values from 0-0.7, yellow till 0.8 and green till unity. The spinal cords DSC values are not representative due to the fact that physicians may not always contour the entire structure. Abbreviations of structures are expanded in table 3–1.

Patient	Applicator	Bladder	CTV	Rectum	Mean	Stdev
GYN01	0.92	0.66	0.82	0.79	0.80	0.11
GYN02	0.83	0.80	0.86	0.66	0.79	0.09
GYN03	0.83	0.81	0.81	0.67	0.78	0.07
GYN04	0.81	0.69	0.75	0.69	0.74	0.06
GYN05	0.84	0.72	0.77	0.73	0.76	0.05
GYN06	0.81	0.71	0.82	0.63	0.74	0.09
GYN07	0.87	0.75	0.81	0.69	0.78	0.08
GYN08	0.81	0.82	0.75	0.77	0.79	0.03
GYN09	0.47	0.59	0.81	0.67	0.64	0.14
GYN10	0.28	0.70	0.56	0.62	0.54	0.18
GYN11	0.80	0.62	0.84	0.76	0.75	0.10
GYN12	0.82	0.68	0.87	0.72	0.77	0.09
GYN13	0.88	0.82	0.90	0.77	0.84	0.06
GYN14	0.77	0.84	0.83	0.62	0.76	0.10
GYN15	0.69	0.83	0.75	0.72	0.75	0.06
GYN16	0.89	0.66	0.89	0.72	0.79	0.12
Mean	0.77	0.73	0.80	0.70		
Stdev	0.17	0.08	0.08	0.05		

Table 3–4: DSC values for various structures for the gynecologic brachytherapy cases using the deformable contour propagation method (VelocityAI only). The cells are red for DSC values from 0-0.7, yellow till 0.8 and green till unity.

The propagated contours for the brain, brainstem, spinal cord, eyes, larynx, mandible, parotids and CTVs were quite similar to the physician-drawn contours with mean DSC values ranging between 0.73-0.98. Spinal cord DSC values are not representative due to the fact that physicians may not always contour the entire structure. The algorithm did not perform well with respect to the esophagus and oral cavity, calculated mean DSC values were 0.6 ± 0.2 and 0.7 ± 0.2, respectively. The algorithm performed reasonably well on the GYN cases with mean DSCs ranging between 0.702-0.804 for the applicator, bladder, rectum and CTV. The applicator and the CTV exhibited DSCs that were quite high except for a few outliers which brought down the mean DSC values; 0.8 ± 0.2 and 0.80 ± 0.08, respectively. The DSC values for the applicator and the CTV fared better than the bladder and rectum since registration of these structures only requires a rigid transformation due to their non-deformable nature.

3.4 Conclusions

3.4.1 Atlas-Based Segmentation

The atlas-based segmentation technique revealed that neither of the software truly outperformed the other. Although MIMvista did fare a bit better than VelocityAI both their contours required manual modification if used for a treatment plan. These tools are very promising since they may reduce total contouring time and can be used to generate a decent first draft of the required clinical volumes.

3.4.2 Deformable Contour Propagation

This study has demonstrated that the use of deformable contour propagation is quite accurate and requires minimal modification for use in a valid treatment plan. The HN cases outperformed the GYN cases primarily due to the fact that the GYN scans are low in contrast and contain highly deformable tissues such as the bladder and rectum. This tool is very promising since is may reduce total contouring time and may be used to generate a quick draft for contouring.

Deformable contour propagation and atlas-based segmentation use the same deformable image registration algorithm yet deformable contour propagation performs automatic segmentation better since it deforms structures from a given patient's older scan. The contour propagation technique is ideal for cases where a patient must be re-planned due to anatomical changes since contouring is a tedious and time-consuming task.

References

[1] DL Pham, CY Xu, and JL Prince. A survey of current methods in medical image segmentation. *"Annu. Rev. Biomed. Eng."*, 2, 2000.

[2] T Vuong, Slobodan Devic, Belal Moftah, Michael Evans, and Ervin B. Podgorsak. High-dose-rate endorectal brachytherapy in the treatment of locally advanced rectal carcinoma: Technical aspects. *Brachytherapy*, 4, 2005.

CHAPTER 4
Adapative Radiation Therapy Using Deformable Electron Density Mapping

Contents

4.1 Introduction

When delivering fractionated radiation treatments the patient volume is assumed to be unchanged over the course of treatment. Yan et al. [1] proposed that after monitoring a number of fractions, treatment plans should be modified to correct for dose prescriptions and patient specific margins, they coined the concept of adaptive radiation therapy (ART). Since the inception of ART, treatments include offline (reaction to imaging is delayed to a subsequent fraction) and online (reaction to imaging is made immediately following imaging) plan re-optimization and dose compensation [5]. Dose accumulation is the method of evaluating the cumulative dosimetry of organs at risk and target volumes.

Dose accumulation is performed using a three-dimensional patient image, deformable image registration and dose recalculation or reconstruction. The first requirement, the three-dimensional patient image, can be obtained throughout the

treatment using in-room CT variants such as the CT on rails [6], CBCT, megavoltage CT (MVCT) on helical Tomotherapy treatment machines [2] and linac-MRI systems [4]. Deformable image registration methods have been developed in order to track the daily motion of individual voxels from the initial planning CT image. Kapatoes et al. [3] demonstrated that the exit fluence detected during treatment and in-room CT imaging may be used to reconstruct the dose distribution in the patient. In this chapter, we recalculated dose distributions on weekly pre-treatment CBCT scans and compared DVHs for various structures.

4.2 Methods and Materials

Weekly pre-treatment CBCT images from a head and neck patient were chosen for this study. The patient was treated with 67.5 Gy in 30 fractions to the GTV and had weekly CBCT images acquired pre-treatment throughout the entire treatment (6 CBCTs). Using VelocityAI, we registered the planning CT to the weekly CBCT images. After deformable registration, the HU in each voxel in the planning CT is mapped to the corresponding point in the CBCT image to produce the modified CBCT image. The aforementioned method is also known as the deformable electron density mapping (DEDM), coined by Yang et al. [7]. Dose distributions were then recalculated on the modified CBCT images using the Eclipse treatment planning system (Varian Medical Systems, Inc., Palo Alto, California).

4.2.1 Uncertainty in the Deformable Electron Density Mapping Method

Many factors contribute to the uncertainty in the evaluation of the recalculated dose distribution using the modified CBCT image. For our purposes, we are only interested in errors stemming from interpolation of deformable registration doses and inaccurate image registrations. To observe the magnitude of these effects we scanned and planned the Rando head and neck phantom (Alderson Research

Laboratories, Stamford, CT) and acquired a CBCT scan. Next, we compared a DVH of a target volume from the planning CT to the recalculated dose distribution using the modified CBCT (explained in section 4.2).

4.3 Results and Discussion

4.3.1 Phantom Study

The Rando head and neck phantom was scanned using the CT and CBCT scanners. Figure 4–1 shows an axial and a sagittal image for each imaging modality.

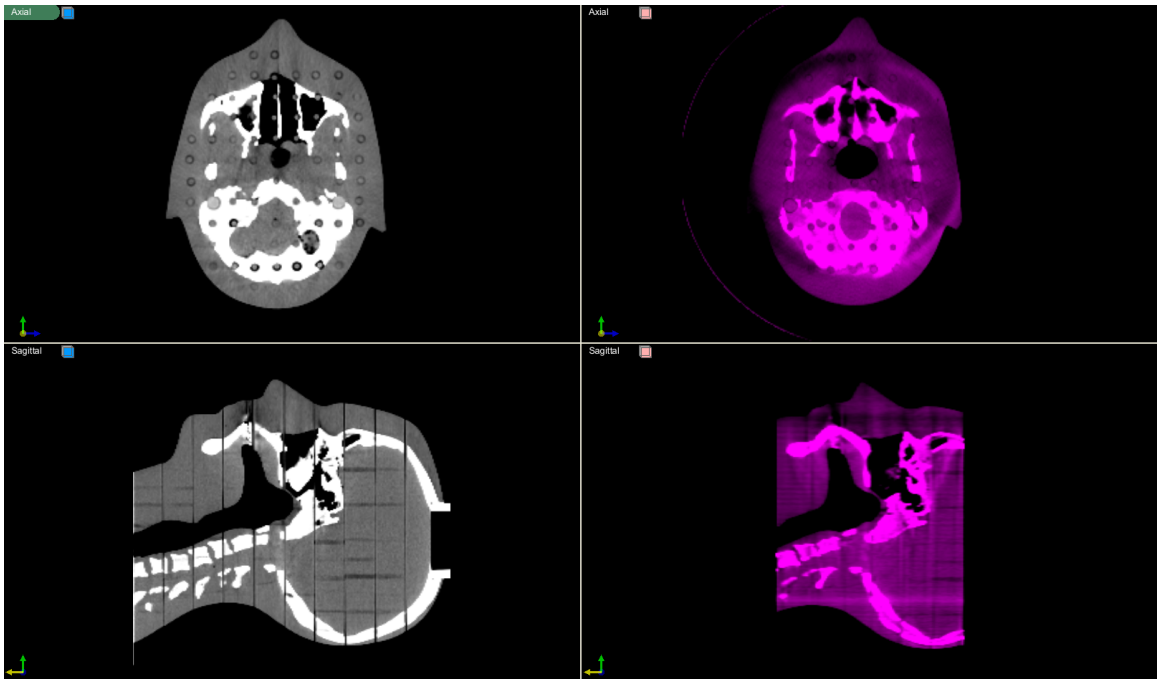

Figure 4–1: Axial and sagittal images from CT (left) and CBCT (right) scans of the Rando head and neck phantom (Alderson Research Laboratories, Stamford, CT).

The CT image was planned using Eclipse. The plan consisted of one 10x10 cm^2 field, 6 MV photon beam, anterior to the target volume which was defined as the palate, found in the roof of the mouth. Once the planning CT had

its dose distribution calculated in Eclipse, the Dose warping is a dose accumulation method where the initial dose distribution is warped on to treatment images to permit the comparison of planned and delivered doses in a common reference frame.

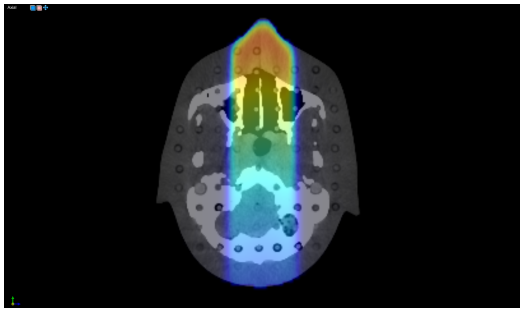

(a) Planning CT

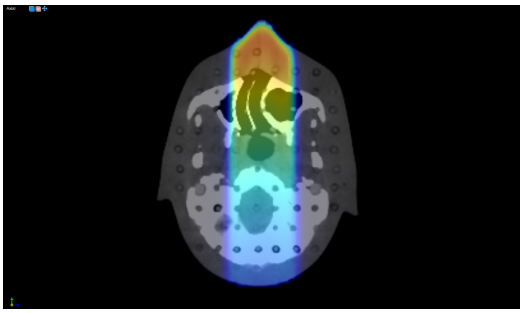

(b) Dose recalculated on modified CBCT

Figure 4–2: Calculated dose distributions for the planning CT (a) and the modified CBCT (b).

The planning CT and the modified CBCT along with their respective dose distributions are shown in figures 4–2(a) and 4–2(b), respectively. The target volume DVHs for both plans are shown in figure 4–3.

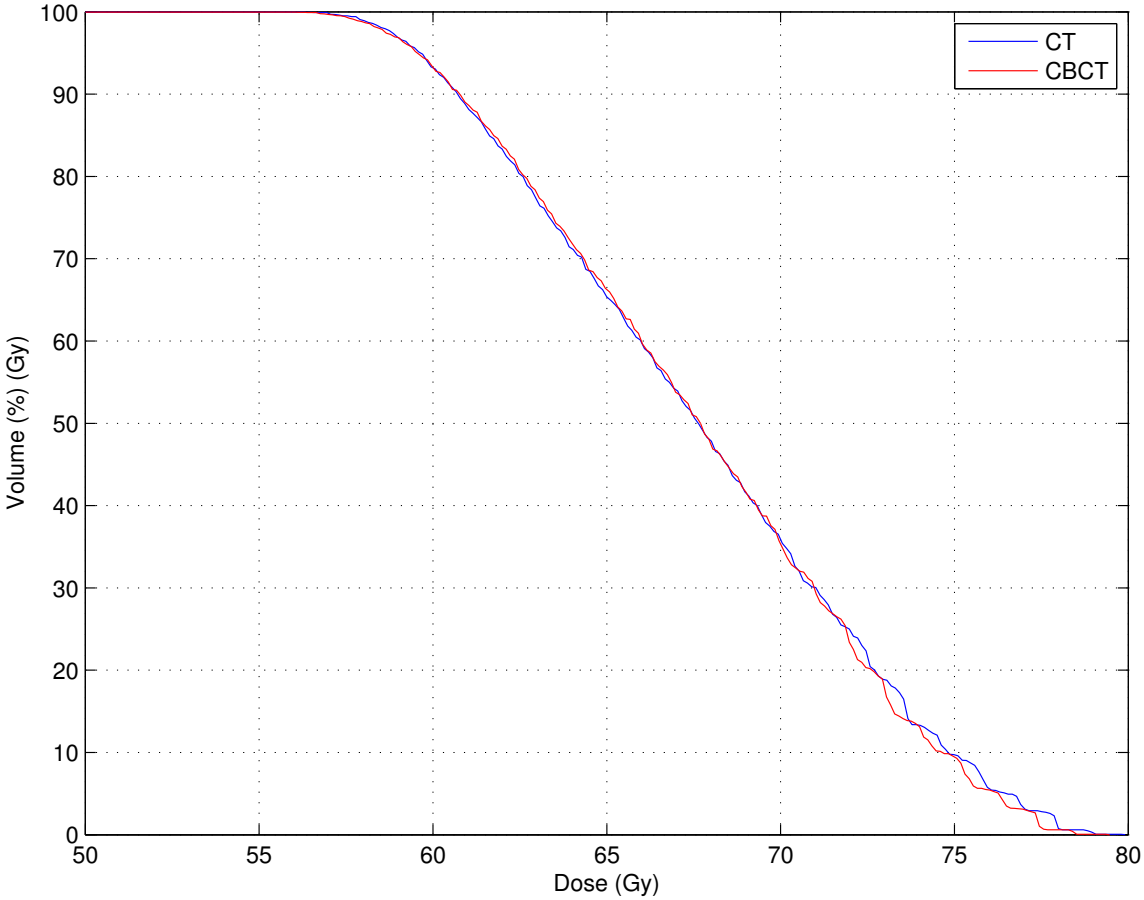

Figure 4–3: DVH of target volume for planning CT and modified CBCT plans.

The DVHs for both plans are in excellent agreement with an average percent error of 0.4%. Deformable electron density mapping seems to work reasonably well for the rigid, Rando phantom case. In the next section we will apply the same principles to a real patient study, where organ deformations occur readily.

4.3.2 Patient Study

Figure 4–4 shows the DVHs for the CTV, spinal cord and right parotid for the planning CT and the six weekly CBCTs for a head and neck patient. Figures 4–5, 4–7 and 4–9 are close ups of the DVHs for each structure, respectively, and figures 4–6, 4–8 and 4–10 are the respective plots of the DVH differences between the weekly CBCTs and the planning CT. The structures in the CBCT

were automatically contoured using the deformable contour propagation method described in chapter 3; the structure set from the original planning CT was deformed to the weekly CBCT scans.

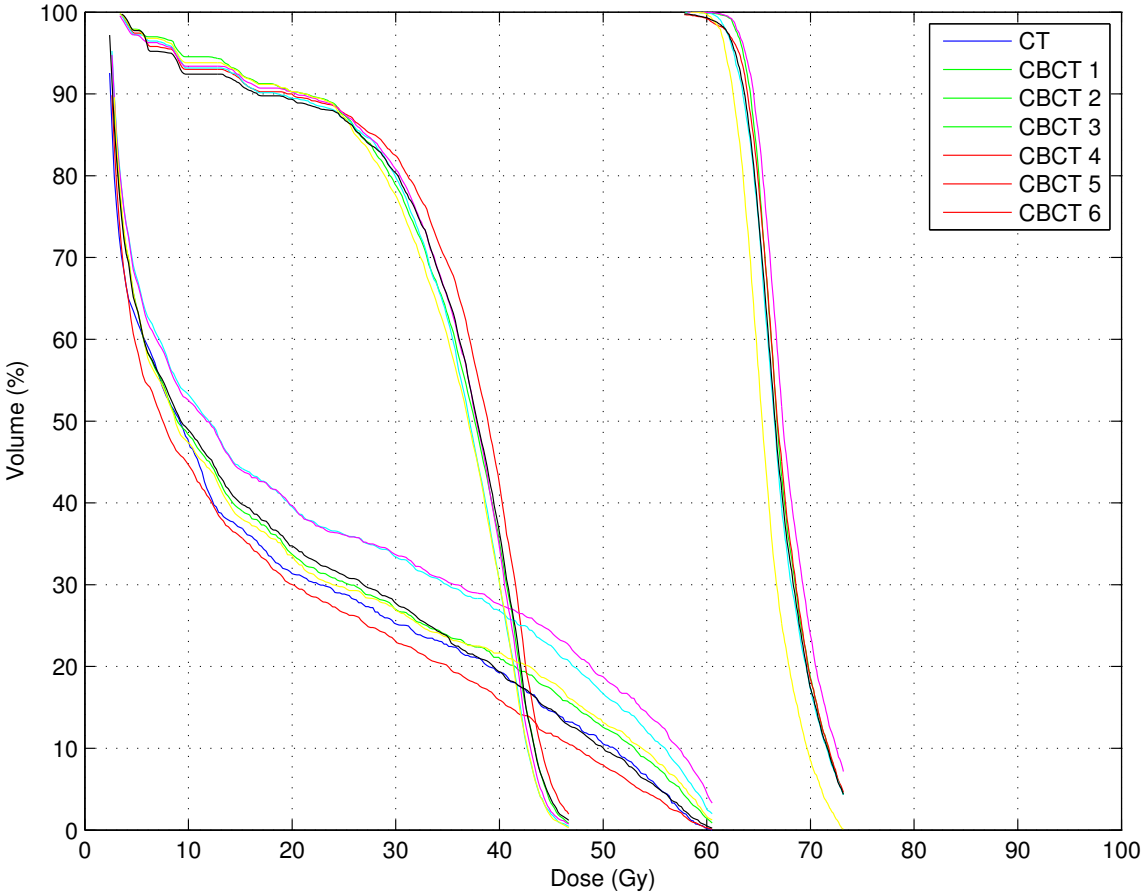

Figure 4–4: DVH of the CTV (rightmost set of curves), spinal cord (middle set of curves) and right parotid (leftmost set of curves) for the planning CT and the six weekly CBCTs.

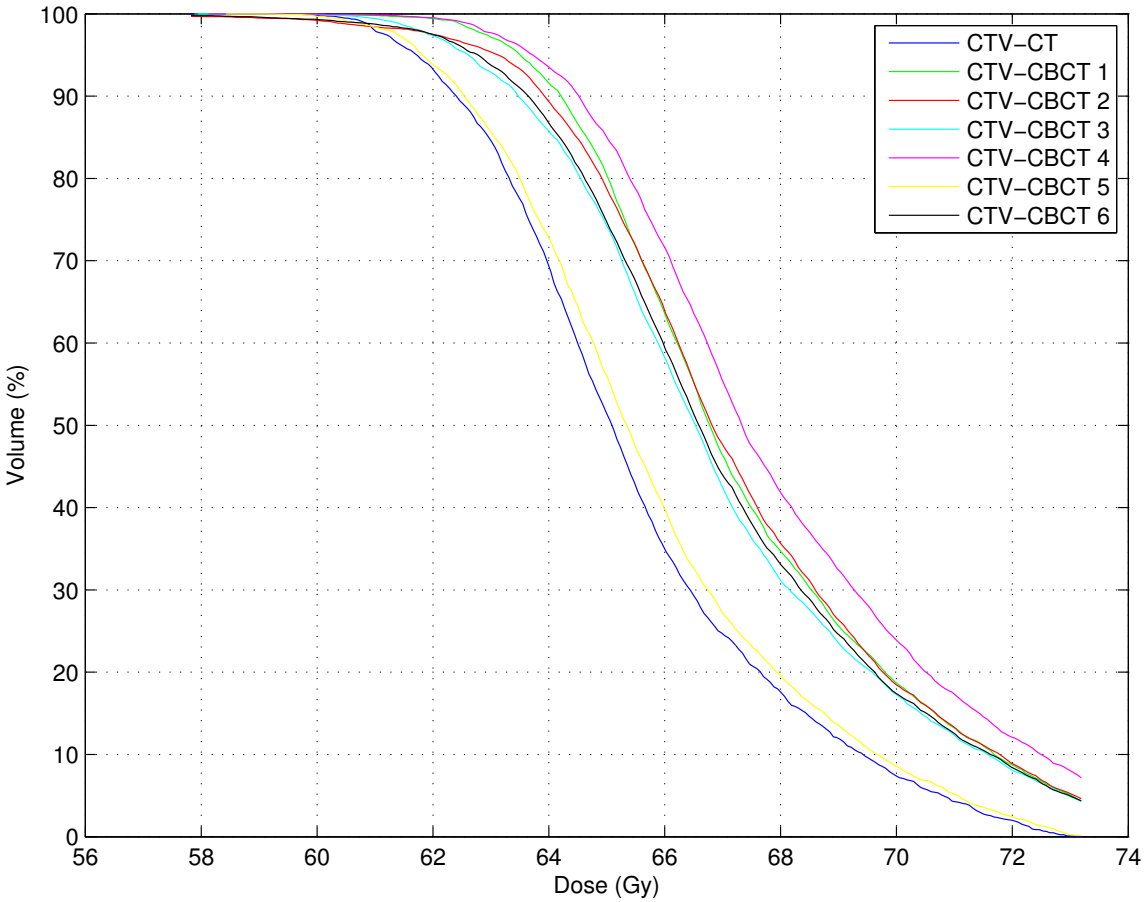

Figure 4–5: DVH of the CTV for the planning CT and the six weekly CBCTs.

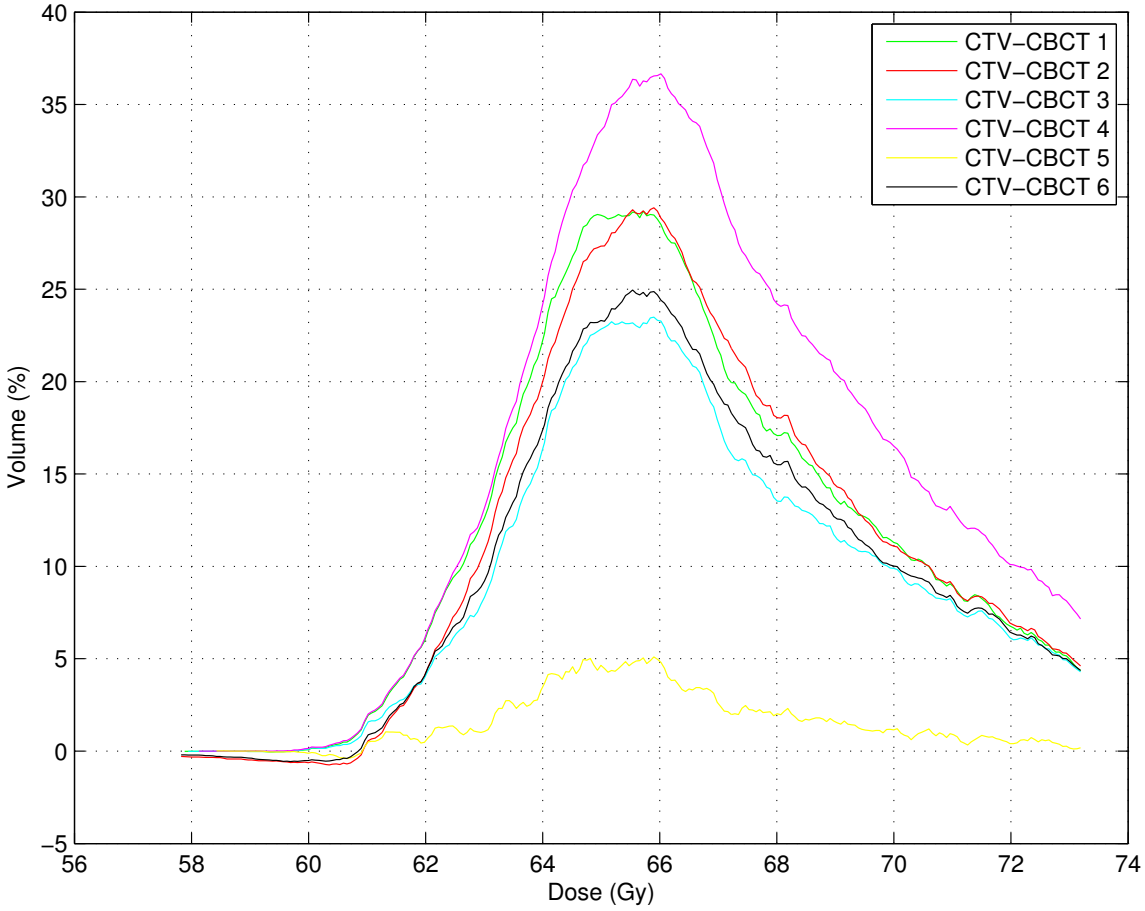

Figure 4–6: Difference in the CTV DVH between each weekly CBCT and the planning CT.

	CT	CBCT 1	CBCT 2	CBCT 3	CBCT 4	CBCT 5	CBCT 6
D_{95}(GY)	61.7	63.5	63.1	62.6	63.7	61.8	62.8
% Error	–	2.8	2.2	1.4	3.2	0.1	1.7

Table 4–1: Doses received by atleast 95% of the CTV volume.

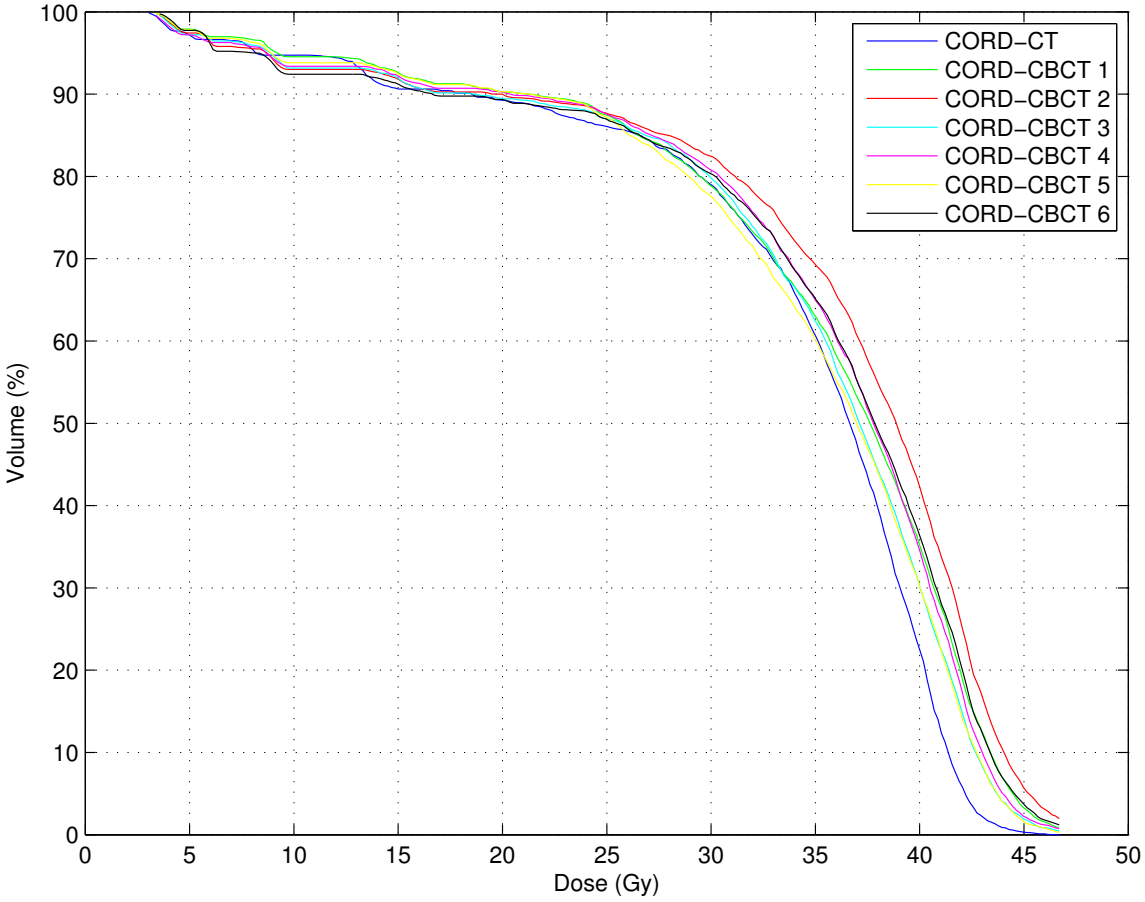

Figure 4–7: DVH of the spinal cord for the planning CT and the six weekly CBCTs.

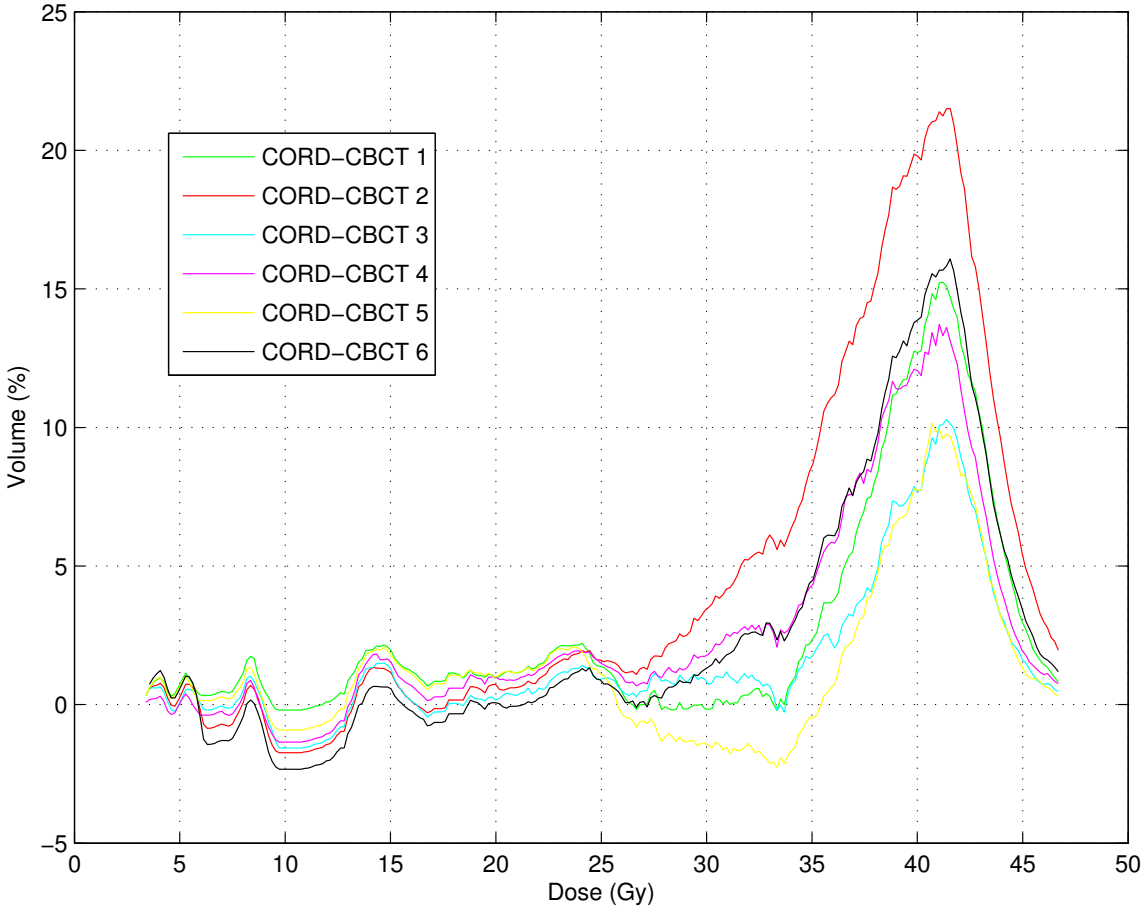

Figure 4–8: Difference in the spinal cord DVH between each weekly CBCT and the planning CT.

	CT	CBCT 1	CBCT 2	CBCT 3	CBCT 4	CBCT 5	CBCT 6
D_{10}(GY)	41.4	43.4	44.1	42.8	42.9	42.8	43.4
% Error	–	5.0	6.6	3.3	3.7	3.3	5.0

Table 4–2: Doses received by atleast 10% of the spinal cord volume.

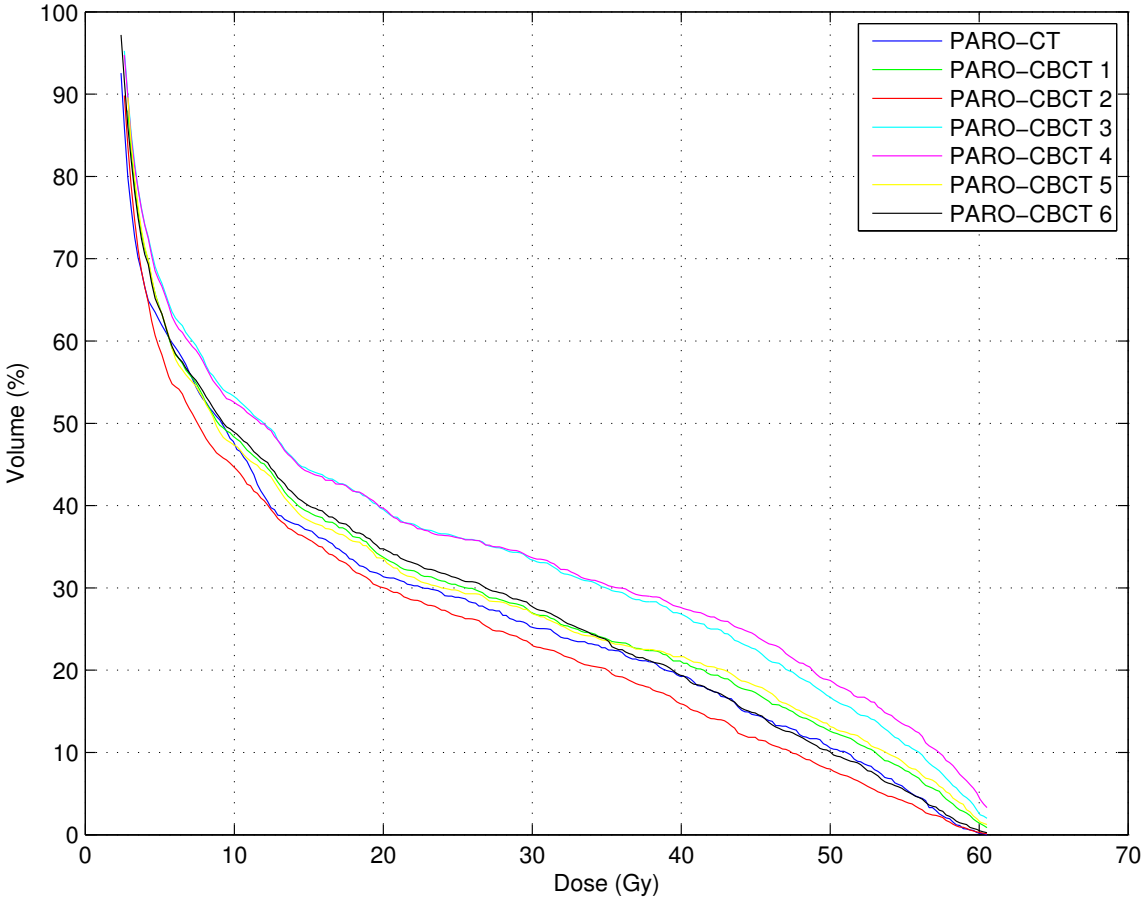

Figure 4–9: DVH3 of the right parotid for the planning CT and the six weekly CBCTs.

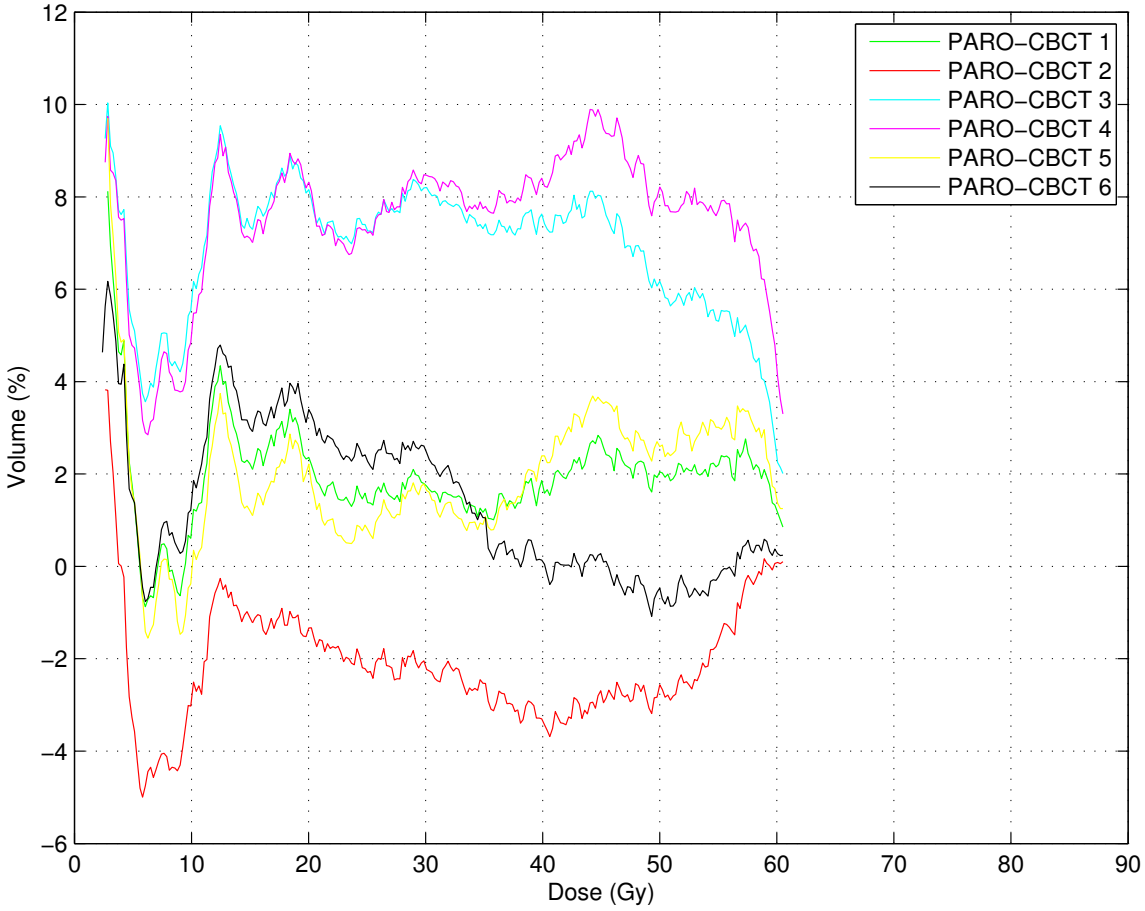

Figure 4–10: Difference in the right parotid DVH between each weekly CBCT and the planning CT.

	CT	CBCT 1	CBCT 2	CBCT 3	CBCT 4	CBCT 5	CBCT 6
D_{10}(GY)	51.1	53.0	47.5	55.9	57.3	53.7	50.0
% Error	–	3.6	-7.2	9.4	12.1	4.9	-2.2

Table 4–3: Doses received by atleast 10% of the right parotid volume.

In comparing planned and delivered doses we demonstrated that a fractionated treatment is not necessarily delivered as planned. The original plan's DVH for the CTV required at least 95% of the volume (D_{95}) to receive 61.5 Gy. The plan recalculation on the CBCTs gave rise to D_{95} values ranging from 61.8 to 63.7 Gy or a percent error ranging from 0.1 to 3.2%. The spinal cord CBCT D_{10} values (10%

of volume to receive at most D_{10}) ranged from 42.8 to 44.1 Gy or a percent error ranging from 3.3 to 6.6%, the original plan's D_{10} was 41.4 Gy. The right parotid exhibited the largest variations with D_{10} ranging from 47.5 to 57.3 Gy or a percent error ranging from -7.2 to 12.1 Gy relative to the original plan's D_{10} value of 51.1 Gy.

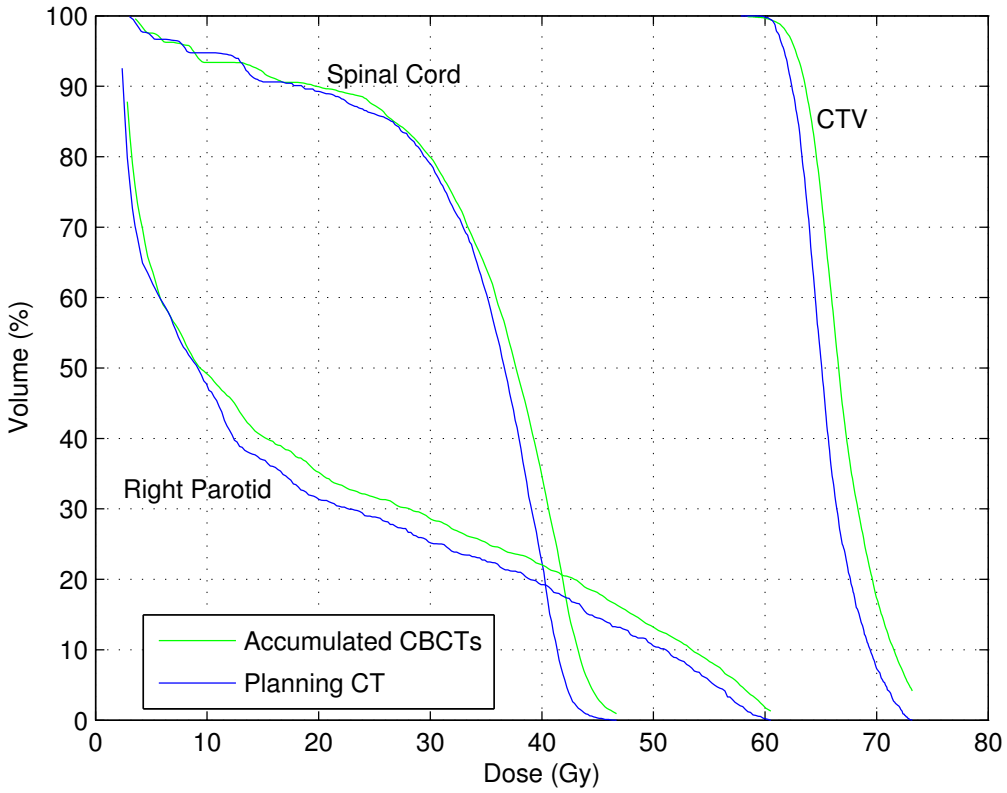

Figure 4–11: DVH of the CTV, spinal cord and right parotid for the planning CT and the accumulated weekly CBCTs.

In figure 4–11, the DVHs for the weekly CBCTs were accumulated and the result was plotted against the original planning CT's DVHs. The accumulated DVH for the CTV yielded a D_{95} of 62.8 Gy or a percent error or 1.8%. The

accumulated DVH for the spinal cord and the right parotid produced D_{10} values of 43.3 and 53.4 Gy or percent errors of 4.6 and 4.5%, respectively.

4.4 Conclusions

Pre-treatment CBCT imaging provides useful information for patient positioning and dose verification. The deformable electron density mapping was an attractive method for calculating dose distributions from the CBCT images since a reliable relationship between the HU and the relative electron density is needed to calculate dose distributions. Our phantom study indicated that the dosimetric accuracy of CBCT-based dose calculation is acceptable for the purpose of dosimetric checks. The patient study has shown that the delivered doses are not necessarily delivered as planned and the differences in the DVH curves varied from fraction to fraction.

References

[1] Yan D, Vicini F, Wong J, and Martinez A. Adaptive radiation therapy. *Phys Med Biol.*, 42, 1997.

[2] Lisa J. Forrest, Thomas Rockwell Mackie, Ken Ruchala, Michelle Turek, Jeff Kapatoes, Hazim Jaradat, Susanta Hui, John Balog, David M. Vail, and Minesh P. Mehta. The utility of megavoltage computed tomography images from a helical tomotherapy system for setup verification purposes. *International journal of radiation oncology*, 60, 2004.

[3] Kapatoes JM, Olivera GH, Ruchala KJ, Smilowitz JB, Reckwerdt PJ, and Mackie TR. A feasible method for clinical delivery verification and dose reconstruction in tomotherapy. *Med Phys.*, 28, 2001.

[4] M Lamey, B Burke, E Blosser, S Rathee, N De Zanche, and B G Fallone. Radio frequency shielding for a linac-mri system. *Physics in Medicine and Biology*, 55(4):995, 2010.

[5] Yu Lei and Qiuwen Wu. A hybrid strategy of offline adaptive planning and online image guidance for prostate cancer radiotherapy. *Physics in Medicine and Biology*, 55, 2010.

[6] C.M. Charlie Ma and Kamen Paskalev. In-room ct techniques for image-guided radiation therapy. *Medical dosimetry*, 31, 2006.

[7] Yong Yang, Eduard Schreibmann, Tianfang Li, Chuang Wang, and Lei Xing. Evaluation of on-board kv cone beam ct (cbct)-based dose calculation. *Physics in Medicine and Biology*, 52, 2007.

CHAPTER 5
Conclusions and Future Work

Contents

5.1 Evaluation of Atlas-Based Segmentation and Deformable Contour Propagation

The atlas-based segmentation technique revealed neither VelocityAI nor MIMvista truly outperformed the other, both their contours required manual modifications if their structures were to be used for treatment planning. Deformable contour propagation was quite accurate relative to atlas-based segmentation due to the fact that a patient's initial planning contours were deformed to a subsequent scan; the patient's initia3l planning contours serve as an excellent starting point for the segmentation. The premise for these tools are very promising since they may considerably reduce contouring time [1] and should reduce variability between contouring experts [3].

5.2 Adapative Radiation Therapy Using Deformable Electron Density Mapping

Pre-treatment 3D treatment imaging not only allows for daily image guidance [2], but in combination with deformable registration and dose calculation tools, can be used to account for daily anatomical variations in the evaluation of cumulative treatment dosimetry. In chapter 4, we developed a framework for dose

accumulation in head and neck adaptive radiation therapy. By registering the planning CT to the weekly CBCT images, we were able to produce modified CBCT images which possess CT Hounsfield units; this was achieved by used deformable image registration. In using our method to compare planned and delivered doses, we concluded that deformable electron density mapping is a feasible technique to allow dose distributions to be recalculated on pre-treatment CBCT scans.

5.3 Future Work

Areas of future research include increasing patient atlas size and attempting the aforementioned automatic segmentation methods with different deformable image registration algorithms. Development of an automatic offline plan-checking system utilizing the CBCTs to evaluate the cumulative dosimetry would also be of great interest.

References

[1] Olivier Commowick, Vincent Grégoire, and Grégoire Malandain. Atlas-based delineation of lymph node levels in head and neck computed tomography images. *Radiotherapy and oncology : journal of the European Society for Therapeutic Radiology and Oncology*, 87, 2008.

[2] Inga S. Grills, Geoffrey Hugo, Larry L. Kestin, Ana Paula Galerani, K. Kenneth Chao, Jennifer Wloch, and Di Yan. Image-guided radiotherapy via daily online cone-beam ct substantially reduces margin requirements for stereotactic lung radiotherapy. *International journal of radiation oncology, biology, physics*, 70, 2008.

[3] Xiao Han, Mischa Hoogeman, Peter Levendag, Lyndon Hibbard, David Teguh, Peter Voet, Andrew Cowen, and Theresa Wolf. Atlas-based auto-segmentation of head and neck ct images. In Dimitris Metaxas, Leon Axel, Gabor Fichtinger, and Gbor Szkely, editors, *Medical Image Computing and Computer-Assisted Intervention MICCAI 2008*, volume 5242 of *Lecture Notes in Computer Science*, pages 434–441. Springer Berlin / Heidelberg, 2008.

ABBREVIATIONS

1D	One-dimension
2D	Two-dimension
3D	Three-dimension
3D-CRT	Three-Dimension Conformal Radiotherapy
EBRT	External beam radiotherapy
GB	Gigabyte
GHz	Gigahertz
GTV	Gross tumor volume
Gy	Gray
ICRU	International Commission on Radiation Units and Measurements
IMRT	Intensity Modulated Radiation Therapy
LINAC	Linear accelerator
MB	Megabyte
MHz	Megahertz
MLC	Multileaf collimator
MRI	Magnetic Resonance Imaging
NTCP	Normal tissue complication probability
PTV	Planning target volume
RF	Radio-frequency
TCP	Tumor control probability
TPS	Treatment planning system
UTCP	Uncomplicated tissue control probability

REFERENCES

[1] Schaly B, Kempe JA, Bauman GS, Battista JJ, and Van Dyk J. Tracking the dose distribution in radiation therapy by accounting for variable anatomy. *Phys Med Biol*, 49, 2004.

[2] WD Bidgood and SC Horii. "introduction to the acr-nema dicom standard". *Radiographics*, 12, 1992.

[3] Rodney A. Brooks. A quantitative theory of the hounsfield unit and its application to dual energy scanning. *Journal of Computer Assisted Tomography*, 1, 1977.

[4] Sha X. Chang, Timothy J. Cullip, and Katharin M. Deschesne. Intensity modulation delivery techniques: "Step & shoot" mlc auto-sequence versus the use of a modulator. *Medical Physics*, 27, 2000.

[5] Olivier Commowick, Vincent Grégoire, and Grégoire Malandain. Atlas-based delineation of lymph node levels in head and neck computed tomography images. *Radiotherapy and oncology : journal of the European Society for Therapeutic Radiology and Oncology*, 87, 2008.

[6] W R Crum. Non-rigid image registration: theory and practice. *British Journal of Radiology*, 77, 2004.

[7] Yan D, Jaffray DA, and Wong JW. A model to accumulate fractionated dose in a deforming organ. *Int J Radiat Oncol Biol Phys*, 44, 1999.

[8] Yan D, Vicini F, Wong J, and Martinez A. Adaptive radiation therapy. *Phys Med Biol.*, 42, 1997.

[9] Lee R. Dice. Measures of the amount of ecologic association between species. *Ecology*, 26, 1945.

[10] Lisa J. Forrest, Thomas Rockwell Mackie, Ken Ruchala, Michelle Turek, Jeff Kapatoes, Hazim Jaradat, Susanta Hui, John Balog, David M. Vail, and Minesh P. Mehta. The utility of megavoltage computed tomography images from a helical tomotherapy system for setup verification purposes. *International journal of radiation oncology*, 60, 2004.

[11] Hounsfield G.N. Computerized transverse axial scanning (tomography): Part 1. description of system. *British J Radiology*, 46, 1973.

[12] L Gottesfeld Brown. A survey of image registration techniques. *ACM Computing Surveys CSUR*, 24, 1992.

[13] Inga S. Grills, Geoffrey Hugo, Larry L. Kestin, Ana Paula Galerani, K. Kenneth Chao, Jennifer Wloch, and Di Yan. Image-guided radiotherapy via daily online cone-beam ct substantially reduces margin requirements for stereotactic lung radiotherapy. *International journal of radiation oncology, biology, physics*, 70, 2008.

[14] Intensity Modulated Radiation Therapy Collaborative Working Group. Intensity-modulated radiotherapy: current status and issues of interest. *Int J Radiat Oncol Biol Phys*, 4, 2001.

[15] Xiao Han, Mischa Hoogeman, Peter Levendag, Lyndon Hibbard, David Teguh, Peter Voet, Andrew Cowen, and Theresa Wolf. Atlas-based auto-segmentation of head and neck ct images. In Dimitris Metaxas, Leon Axel, Gabor Fichtinger, and Gbor Szkely, editors, *Medical Image Computing and Computer-Assisted Intervention MICCAI 2008*, volume 5242 of *Lecture Notes in Computer Science*, pages 434–441. Springer Berlin / Heidelberg, 2008.

[16] Jaffray DA, Bissonnette JP, Craig T. *X-ray Imaging for Verification and Localization in Radiation Therapy in Modern Technology of Radiation Oncology (suppl. 1). Modern Technology of Radiation Oncology.* Medical Physics Publishing, 1999.

[17] Geneviève Jarry, Sean A. Graham, Douglas J. Moseley, David J. Jaffray, Jeffrey H. Siewerdsen, and Frank Verhaegen. Characterization of scattered radiation in kv cbct images using monte carlo simulations. *Medical Physics*, 33, 2006.

[18] Kapatoes JM, Olivera GH, Ruchala KJ, Smilowitz JB, Reckwerdt PJ, and Mackie TR. A feasible method for clinical delivery verification and dose reconstruction in tomotherapy. *Med Phys.*, 28, 2001.

[19] Joakim Jonsson, Magnus Karlsson, Mikael Karlsson, and Tufve Nyholm. Treatment planning using mri data: an analysis of the dose calculation accuracy for different treatment regions. *Radiation Oncology*, 5, 2010.

[20] Faiz M. Khan. *The Physics of Radiotherapy.* Lippincott Williams & Wilkins, third edition, 2003.

[21] Langen KM, Meeks SL, Poole DO, Wagner TH, Willoughby TR, Kupelian PA, Ruchala KJ, Haimerl J, and Olivera GH. The use of megavoltage ct (mvct) images for dose recomputations. *Phys Med Biol*, 50, 2005.

[22] M Lamey, B Burke, E Blosser, S Rathee, N De Zanche, and B G Fallone. Radio frequency shielding for a linac-mri system. *Physics in Medicine and Biology*, 55(4):995, 2010.

[23] Yu Lei and Qiuwen Wu. A hybrid strategy of offline adaptive planning and online image guidance for prostate cancer radiotherapy. *Physics in Medicine and Biology*, 55, 2010.

[24] C.M. Charlie Ma and Kamen Paskalev. In-room ct techniques for image-guided radiation therapy. *Medical dosimetry*, 31, 2006.

[25] Jasper Nijkamp, Floris J. Pos, Tonnis T. Nuver, Rianne de Jong, Peter Remeijer, Jan-Jakob Sonke, and Joos V. Lebesque. Adaptive radiotherapy for prostate cancer using kilovoltage cone-beam computed tomography: First clinical results. *Radiotherapy and oncology : journal of the European Society for Therapeutic Radiology and Oncology*, 70, 2008.

[26] International Commission on Radiation Units and Measurements. ICRU Report 50: Prescribing, recording, and reporting photon beam therapy. *International Commission on Radiation Units and Measurements*, 1993.

[27] International Commission on Radiation Units and Measurements. ICRU Report 62: Prescribing, recording and reporting photon beam therapy (supplement to icru report 50). *International Commission on Radiation Units and Measurements*, 1999.

[28] International Commission on Radiation Units and Measurements. ICRU Report 71: Prescribing, recording, and reporting electron beam therapy. *International Commission on Radiation Units and Measurements*, 2004.

[29] International Commission on Radiation Units and Measurements. ICRU Report 78: Prescribing, recording, and reporting proton beam therapy. *International Commission on Radiation Units and Measurements*, 2007.

[30] International Commission on Radiation Units and Measurements. ICRU Report 83: Prescribing, recording, and reporting photon-beam intensity-modulated radiation therapy (imrt). *International Commission on Radiation Units and Measurements*, 2007.

[31] DL Pham, CY Xu, and JL Prince. A survey of current methods in medical image segmentation. *"Annu. Rev. Biomed. Eng."*, 2, 2000.

[32] Josien P W Pluim, J B Antoine Maintz, and Max a Viergever. Mutual-information-based registration of medical images: a survey. *IEEE transactions on medical imaging*, 22, 2003.

[33] D Rueckert, L I Sonoda, C Hayes, D L Hill, M O Leach, and D J Hawkes. Nonrigid registration using free-form deformations: application to breast MR images. *IEEE transactions on medical imaging*, 18, 1999.

[34] Ana Irene Ramrez Galarza & José Seade. *Introduction to classical geometries*. Birkhauser, 2007.

[35] T Vuong, Slobodan Devic, Belal Moftah, Michael Evans, and Ervin B. Podgorsak. High-dose-rate endorectal brachytherapy in the treatment of locally advanced rectal carcinoma: Technical aspects. *Brachytherapy*, 4, 2005.

[36] G.R.J. Swennen W. De Vos, J. Casselman. Cone-beam computerized tomography (cbct) imaging of the oral and maxillofacial region: A systematic review of the literature. *International journal of oral and maxillofacial surgery*, 38, 2009.

[37] Simon K Warfield, Kelly H Zou, and William M Wells. Simultaneous truth and performance level estimation (STAPLE): an algorithm for the validation of image segmentation. *IEEE transactions on medical imaging*, 23, 2004.

[38] S Webb. The physical basis of imrt and inverse planning. *British Journal of Radiology*, 76, 2003.

[39] Yong Yang, Eduard Schreibmann, Tianfang Li, Chuang Wang, and Lei Xing. Evaluation of on-board kv cone beam ct (cbct)-based dose calculation. *Physics in Medicine and Biology*, 52, 2007.

[40] B Zitova. Image registration methods: a survey. *Image and Vision Computing*, 21, 2003.